Title

Impact of hygrothermal aging on rotational behavior of web-flange junctions of structural pultruded composite members for bridge applications

Authors

Haohui Xin

Mosallam, AS

Liu, Y

Publication Date

2023-12-11

Peer reviewed

HYGROTHERMAL AGING EFFECTS ON AXIAL BEHAVIOR OF PULTRUDED WEB-FLANGE JUNCTIONS AND ADHESIVELY-BONDED BUILT-UP BRIDGE COMPOSITE MEMBERS

Haohui Xin[a], Ayman Mosallam[b], Yuqing Liu[a]*, Congzhe Wang[a], Youyou Zhang[c]

[a] Department of Bridge Engineering, Tongji University, Shanghai, China
[b] Department of Civil and Environment Engineering, University of California, Irvine, CA,USA
[c] Department of Civil and Environmental Engineering, University of California, Davis, CA,USA
** Corresponding author. Tel.: +86 21 65983116; Fax: +86 21 65983450*
E-mail: yql@tongji.edu.cn

ABSTRACT

In terms of the unidirectional characteristics of the majority of unstiffened open-web pultruded fiber reinforced polymer (PFRP) composites profiles, local failure of matrix-rich web/flange junctions (WFJ) are inescapable due to lack of fiber continuity at WFJs. Strength and stiffness of WFJ, greatly affect PFRP structure's overall strength, its buckling and post-buckling behavior, as well as reliability of framing connections especially under harsh service environments. In this paper, the axial mechanical behavior of WFJs of pultruded bridge deck components before and after hygrothermal aging effect is assessed. In the experimental phase, axial tensile tests on six different types of pultruded web-flange junctions were performed to investigate axial characteristics of such junctions. In order to evaluate the hygrothermal behavior of such junctions, axial tensile tests were conducted on WFJ specimens that were exposed to fresh water and artificial seawater at temperatures of 40℃, 60℃, and 80℃. Several controlling parameters affecting strength and stiffness of pultruded WFJs including: (i) WFJ's web and flange thicknesses, (ii) fillet radius, and (iii) variation of hygrothermal environments are evaluated and discussed.

To date, there is no design limit state for pultruded composites that includes the premature failure of web-flange junctions of pultruded composite profiles. This issue was highlighted by the second author during the development of the ASCE Standard Document for Structural Design of Pultruded Composites that is currently being developed in USA. It is hoped that the experimental results obtained from this multi-phase study could provide foundation of establishing a limit-state design guide that includes the inherent deficiency of web/flange junctions of PFRP structures to ensure safe and reliable design of such structures. Results of this study indicated that the larger web thickness, the larger flange thickness and the larger fillet radius may contribute to a larger axial tensile capacity of pultruded profiles. Results also showed that increasing the web thickness, flange thickness and fillet radius may not proportionally guarantee the achievement of larger axial tensile load capacity and stiffness of web-flange junction due to common rich resin areas, fabric fold and misalignment effects (refer to Figures 3 and 4). Results also indicated that the degradation of WFJ's axial strength is relatively larger when exposed to higher temperatures. In addition, experimental results showed that there is a slight difference on WFJ axial strength degradation when specimens were exposed to fresh water or artificial seawater environments.

KEYWORDS: A. Polymer-matrix composites; A. Laminates; B. Environmental degradation; E. Pultrusion

1. INTRODUCTION

In terms of high strength, light-weight, corrosion resistance and continuous manufacturing features, pultruded fiber reinforced polymer (PFRP) composites have been used in several successful applications both in newly constructed facilities applications [1-3] as well as repairing deteriorated structures [4-6]. For new structures, commercially produced, steel-like, unidirectional pultruded profiles are commonly used including H-girders [7-9], double-web beam girders [10-11], hybrid FRP-concrete girders [12], box girders [13], stay-in-place (SIP) FRP-concrete hybrid deck as [14-16], as well as sandwich bridge decks [17-18].

Understanding and designing in response to micromechanical behavior of the web-flange junction is critical to the successful application of PFRP composite connections. The premature local failure of web-flange junctions (WFJs) [19-20] is shown in Fig. 1 and Fig. 2. This premature failure is due to existence of rich resin areas that is commonly lack fiber continuity and fabric fold between flange and web as shown in Fig. 3 and Fig. 4 [21]. Previous research [21-28] showed that the existence of such under-reinforced weak regions greatly influence both strength and stiffness of the open-web local structural member and consequently the global behavior of the pultruded structure as well as framing connections, durability and buckling and post-buckling behavior. There are two potential locations where local failure of pultruded WFJs were observed and identified by previous studies [21]: (i) at regions of pultruded girders or columns with highest compressive stresses (refer to Figure 1-a), and (ii) at framing connections where high tensile stresses are generated at open-web columns' flanges at the connection region (refer to Figure 1-b).

In the past few decades, several studies were performed to investigate mechanical performance of pultruded web-flange junctions. A pioneering study was reported by Mosallam et al. [21] on the results of a pilot experimental study that focused on evaluating both axial and rotational stiffness of pultruded H- and L-profiles tested under both service and ultimate loads. Load-displacement (P-δ) and moment-rotation (M-θ) relations were experimentally developed for different pultruded specimens in order to accurately model and establish design limit-state of PFRP members. Feo et al. [7] conducted experimental and numerical studies on assessing the behavior web-flange junctions of pultruded I- profiles. Experimental results indicated that WFJ strength depends on location of the applied pull force and that the loaded length is dependent on the influence zone. Bank et al. [22-23] experimentally and numerically studied the influence of web-flange junction's strength and stiffness on local and global buckling of pultruded I-beam. The tests results showed that significant increases in load carrying capacity of pultruded beams can be achieved with minor geometry and fiber architecture modifications. A node-separation technique is used to simulate the progressive failure of the joint between the flange and the web of the wide-flange beam in the post buckled regime. The tensile and shear performance of web-flange joints of wide flange I- profiles were experimentally investigated by Turvey and Zhang [25-27], the results showed that the WFJ of pultruded profiles with smaller flanges have larger tearing strength than those of pultruded profiles with larger flanges and that the shear strength of WFJs are much lower than flat pultruded laminates. Ascione et al. [28] proposed a closed-form equation that considers the contribution of the elastic restraint stiffness of the web–flange junction. The theoretical results were compared with

experimental and numerical data indicating that validity of their proposed theoretical model.

For bridge applications, the structures are constantly exposed to harsh and changing environments and degradations in both mechanical and physical properties of PFRP composite members are expected [29-41]. Figure (5) shows an example of typical extreme bridge wet environment imposed on a pultruded composite deck in USA. For this reason, it is critical to understand the durability of web-flange junctions to ensure reliability of PFRP profiles and to avoid premature failure that has been witnessed in several cases where pultruded composites are exposed to harsh environments. Liao et al. [31] evaluated experimentally the behavior of PFRP materials before and after aging in both fresh water and salt water solutions at temperatures of 25℃ and 75℃. Experimental results indicated the following: (1) both strength and modulus decreased with environmental aging, (2) environmental aging decreased the in-situ fiber strength, and (3) the degradation of fiber/matrix interphase region occurred during the aging period. Due to the fact that all bridge structural members are subjected to cyclic loading, it is critical to understand fatigue performance of pultruded structural members. Fatigue behavior of PFRP materials was also assessed by Liao et al. [32]. In this study, flexural (four-point bending) fatigue behavior of PFRP specimens was evaluated when exposed to various environments such as fresh and salt water solutions containing mass fractions of either 5% NaCl or 10% NaCl. All specimens were aged for periods up to 6,570 hours (9.0 months). Iqbal [33] reported results of a comprehensive study that focused on fatigue life of two types of E-glass/phenolic GFRP including hand lay-up and pultruded composites with special emphasis on the effect of environmental degradation on the fatigue life such materials.

In this study, fatigue tests were performed at constant amplitude with a frequency of 20.0Hz, and S-N curves were developed for each exposure group. The results show that, except for UV weathering, the fatigue life of all the exposed composite specimens exhibited slight statistically significant improvement for low stress fatigue tests. In addition, residual strength tests conducted at 10% of ultimate strength exhibited no statistically significant (α=0.05) reduction in tensile strength or modulus at three million cycles of fatigue loading. Correia et al. [34] conducted an experimental investigation to assess the durability of glass/polyester PFRP profiles that are used for construction applications. In their study, accelerated aging of pultruded profiles was accomplished by exposing composite specimens to different environments including moisture, temperature, and ultraviolet (UV) radiation. Results indicated that considerable chromatic changes were observed, especially when profiles were subjected UV radiation. Experimental results indicated that PFRP fatigue behavior was degraded significantly when aged in water at 75°C for 2,400 hours prior to cyclic test at load levels above 30% of the dry flexural strength. Abanilla et al. [35] investigated the aging properties of CFRP composites exposed to deionized water, salt and alkali water, freeze-thaw and accelerated aqueous environments for a period exceeding 100 weeks. Their experimental results indicated that significant strength degradation occurred due to fiber/matrix interface deterioration, however, a relatively less stiffness degradation was observed. Karbhari and Abanilla [36] used two predictive models to estimate the long-term deterioration of CFRP for a range of material's characteristics and outlined a methodology that is capable of accounting for temperature variation during exposure period. Xin et al. [37] carried out gravimetric tests

to investigate the moisture diffusion characteristic and hygrothermal aging properties in bridge profiles pultruded glass-fiber-reinforced-polymer composite laminates exposed to both fresh and artificial seawater at temperatures of 40℃, 60℃and 80℃. The moisture diffusions were separated into a diffusion-dominated uptake, a polymer relaxation-dominated uptake and a composite damage-dominated uptake. It is impractical to use the exposure period as the design service life of a bridge that last for hundreds of years. For this reason, accelerated experimental methods are generally adopted to simulate the degradation effect [42-43]. In this accelerated process, temperature and/or moisture conditions are raised beyond the normal service conditions to accelerate the expected degradation process.

Although several investigations on T-joints were carried out in the aerospace or mechanical engineering, it is not convincing to directly extend those experimental or numerical results from aerospace and mechanical engineering to civil engineering for several reasons that include: (i) different types of advanced fiber reinforcement used in aerospace applications which is typically in the form of pre-impregnated (pre-pregs), ultra-weight, high-performance and high volume fraction carbon fibers reinforced polymer composites that are usually are manufactured using a more sophisticated manufacturing techniques such as auto-claves, vacuum-assisted transfer molding (VARTM), resin transfer molding (RTM) and other methods that undergo strict quality control/quality assurance (QC/QA) and inspection procedures. In contrast and for economic reasons, E-glass fibers are the common type reinforcement for the majority of civil engineering applications with a relatively lower fiber volume fraction (40% to 50%) with different types of additives that in most cases increase the moisture migration into the pultruded

member especially if no compatible polymeric sealing of the cut edges is employed. The pultrusion process used for producing pultruded profiles for construction application has a relatively lower quality control resulting in uneven and unstable reinforcement distribution. An example of such quality control related issues is what is referred to mat folding as shown in Figure 4. Fabric folds of PFRP WFJs lead to much challenge on the numerical modelling at lamina level, (ii) due to the limited capability of the pultrusion process, it is usually difficult to maintain sufficient fiber continuity and volume between the web(s) and flanges creating the typical matrix-dominated zone (refer to Fig. 3), and (iii) lack of knowledge of the majority of bridge engineering on the behavior, capabilities and limitations (both short- and long-term) of pultruded composites. Based on the information obtained from the in-depth literature review, it is believed that there is a dearth of experimental data related to this subject and, accordingly, a limited set of empirical formulations that consider such inherent deficiencies that is sufficient to provide the basis for safe and reliable structural design and standards for pultruded composite structures.

This study is considered to be one of the pioneering investigations that focus on both short-term and durability as well as hygrothermal effects of web/flange junctions and adhesively-bonded built-up joints of pultruded composite profiles. The objective of the current study is to assess both strength and axial stiffness of web-flange junctions of PFRP bridge profiles and hygrothermal aging effects on its mechanical behavior. This paper presents: (1) experimental results obtained from six different as-built (unexposed) pultruded web-flange junction types and adhesively-bonded joints in order to identify the as-built axial characteristics of such

junctions, and (2) residual strength of one of the WFJs to evaluate the hygrothermal effects when exposed to both fresh and artificial sea water environments at temperatures of 40℃, 60℃ and 80℃. The axial ultimate capacity, a stiffness and failure modes of both un-aged (as-built) and aged (exposed) web-flange junctions (WFJs) were experimentally evaluated. The following sections describe the details and results of the experimental program. The results of this study provides a much needed information that are needed for accurate time-dependent characterization of different pultruded web/flange junctions and bonded built-up structural members for bridge applications.

2 EXPERIMENTAL PROGRAMS

2.1 Specimens Preparation: The six different web-flange junctions (WFJs) evaluated in this study are divided into two groups; (i) web/flange junctions denoted as "*J*- group" and adhesively-bonded joints denoted as "*AJ*- group". It should be noted that WFJ's specimens of the *J*- group are parts of an integrated pultruded composite deck, while the adhesively-bonded joints were fabricated by splicing two independent pultruded profiles forming built-up structural members. The tenon part of adhesive junctions group is denoted as "*AJ#-1*" and the mortise part of adhesive junctions group is denoted as "*AJ#-2*".

Figures (6) and (7) present details of the *J*-group and *AJ*-group specimens evaluated in this study, respectively. It should be noted that in this paper, the pultrusion direction is denoted as 0^0 directions, while direction contains θ degree clockwise with pultrusion direction is denoted as θ^0 direction and direction contains θ degree counter-clockwise with the pultrusion direction is denoted as $-\theta^0$ direction. For *J1* and *AJ1* specimens, both web and flanges have

seven plies with the following reinforcements:(1) 0^0 plies in the form of 9600 Tex E-glass fiber roving, (2) 90^0 plies in the form of unidirectional non-crimp E-glass fabrics, and (3) $\pm45^0$ plies in the form of biaxial non-crimp E-glass fabrics. Each roving layer has 252.25 bunches roving per meter along the cross section. The 90^0 laminas were fabricated based on axial non-crimp fabric with a density of 450 g/m^2 and the $\pm45^0$ lamina were fabricated by biaxial non-crimp fabric with a density of 680 g/m^2. For other junctions and joints specimens, both web and flanges are made of five plies with the following reinforcements: (i) 0^0 plies in the form of 9600 TEX E-glass rovings, and (ii) multi-directional non-crimp E-glass fabrics with three fiber axes serving as 90^0 and $\pm45^0$ plies, which includes 220 g/m^2 fabric with $+45^0$ orientation, 150g/m^2 fabric with 90^0 orientation and 220 g/m^2 fabric with -45^0 orientation. In order to keep the fabric continuity of web and flange, 50 mm long lapped length of fabrics were specially designed.

The dimensions of specimens are listed in Table (1) and the symbols are explained in Figure (8). All specimens were fabricated with same length of flange, a=200 mm, flange width, b_1 = 40 mm, web height, b_2 =40 mm. The web thickness of the *J1* specimen is 6 mm, while the web thickness of both WFJ specimens *J2* and *J3* is 4.5 mm. The web thickness of all adhesively-bonded joints is 12.5 mm. The flange thickness, t_f, of WFJ specimens *J1, J2,* and adhesively-bonded built-up specimens *AJ1* and *AJ2* is 6.0 mm while the flange thickness t_f of WFJ specimen *J3* and adhesively-bonded built-up specimen *AJ3* is 8 mm. The radius of circular arc (fillet) of WFJ specimen *J1* and adhesively-bonded built-up specimen *AJ1* is 10.0 mm. For all other WFJ, fillet radii are increased to 20.0 mm. For all other adhesively-bonded profiles,

fillet radii are increased to 30.0 mm. The joints height, *h*, of WFJ specimen *J1, J2,* and adhesively-bonded built-up specimens *AJ1* and *AJ2* is 106.0mm while the joints height, *h*, of WFJ specimen *J3* and adhesively-bonded built-up specimen *AJ3* is 108.0 mm.

Three identical specimens and total 18 specimens are prepared for each web-flange junction type to investigate axial characteristics prior conducting hygrothermal aging tests (i.e. as-built characterization tests). The WFJs hygrothermal effects tests on axial characteristic of web-flange joints were performed on a total of seventy-two *J1* specimens that were prepared and immersed in the following six different environmental aging conditions: (1) 40℃-W (fresh water), (2) 60℃-W (fresh water), (3) 80℃-W (fresh water), (4) 40℃-SW (artificial seawater), (5) 60℃-SW (artificial seawater). and (6) 80℃-SW (artificial seawater). After 1 weeks, 2 weeks, 3 weeks, 4 weeks, 6 weeks, 12 weeks and 26 weeks aging time, two identical specimens in each environment aging conditions were removed from the environmental chamber, conditioned prior to performing tensile tests. The artificial seawater was prepared by mixing artificial sea salt with water with 3.5% concentration depending on the average global ocean salt concentration. The ingredient and content of sea salt are listed in Table (2). The salt concentrations of each salt water solution chamber were monitored by densitometer and concentration level was adjusted to be approximately 3.5% after each specific time interval.

2.2 Experimental Test Setup: The typical experimental setup is presented in Figure (9). As shown in the figure, each specimen is fixed to a steel plate (300 mm×300 mm×40 mm) using four steel fixtures with a width of 40.0 mm and a thickness of 20.0 mm via with eight 16.00 mm diameter high-strength steel bolts. All web-flange junctions' tensile axial tests were

conducted using a calibrated a calibrated MTS universal testing machine with a capacity of 100.0 kN. During each test, both load and axial displacement measurements were continuously recorded. A displacement-control loading protocol with a constant axial displacement rate of 1.0 mm/min was adopted for all tests. The machine was set to stop when a 40% load drop occurred during the test.

2.3 Materials Properties: The following paragraphs describe experimental procedures used for characterizing both laminate and adhesives mechanical properties.

2.3.1 GFRP Laminates: The tensile, compressive, in-plane shear, flexural and inter-laminar behavior of each laminate were experimentally investigated in accordance to ISO 527-4 [44], ISO 604[45], ISO 14129[46], ISO 14125[47] and ISO 14130[48] standards respectively. In consideration to the anisotropic nature of pultruded composites, five specimens were prepared and tested in both parallel and perpendicular-to-fibers directions. Table (3) presents a summary of mechanical properties of PFRP web and flange laminates.

2.3.2 Adhesives: Two typical stress states exist at for the interface of between the left side and right side of adhesive joints; namely shear and tensile stresses. For this reason, both axial tension and shear properties of the built-up members' bond lines were evaluated experimentally (refer to Figures 10 and 11). A summary of test results is presented in Table (3). As shown in the table, the average tensile strength of epoxy is 5.82 MPa while the average shear strength is 6.09 MPa.

3 EXPERIMENTAL RESULTS AND DISCUSSION ON THE UNEXPOSED (AS-BUILT) SPECIMENS

Figure (12) shows the details of both the trilinear and bilinear models used in this study. As shown in Figure (12), the load and displacement at the end of linear range are denoted as P_l and d_l, respectively. The axial ultimate capacity and corresponding displacement are denoted as P_f and d_f, respectively, while the final failure load and displacement are denoted as P_u and d_u, respectively. In this figure, the average of loads P_l and P_f is defined as P_m. Similarly, the average displacement of d_l and d_f is defined as d_m.

In this study, two web-flange junctions linear stiffness are proposed namely; linear stiffness K_l and average linear stiffness K_m [7, 21]. The proposed average linear stiffness, K_m, is extracted from the load-displacement curves by connecting the origin point with the midpoint with coordinates (P_m, d_m). As shown in Figure (12), the trilinear model begins with linear stiffness K_l and contains three lines by connecting the origin point, the end of linear range point (P_l, d_l), the peak load point (P_f, d_f) and the end point (P_u, d_u) in order, while the bilinear model begins with axial linear stiffness K_m and includes two lines by connecting the origin point, the midpoint (P_m, d_m) and the end point (P_u, d_u) in order.

3.1 Experimental Results of Joints Group: The detailed experimental results of joints group are summarized in Tables (5), (6) and (7). Figure (13) presents the load versus axial displacement curves for the joints group. Failure modes of different joints group are presented in Figure (14).

As shown in these tables and figures, the displacement increased linearly as the load increased

up to an average displacement of 0.45 mm for junction specimen *J1*, 1.34 mm for junction specimen *J2* and 1.37 mm for junction specimen *J3* that occurred at an average load level of 2.93kN for junction specimen *J1*, 7.62kN for junction specimen *J2* and 8.91kN for junction specimen *J3.* Beyond these displacement and load levels, stiffness degradations were observed and load-displacement curves behaved nonlinearly until reaching an average axial displacement of 1.21 mm for junction specimen *J1*, 1.34 mm for junction specimen *J2* and 1.37 mm for junction specimen *J3* that corresponds to 5.0 kN load for junction specimen *J1*, 10.88kN load for junction specimen *J2* and 13.28kN load for junction specimen *J3*. It is noted that the ultimate axial force of junction specimen *J1-1* is much larger than other two of junction specimen *J1*. Beyond this level, local cracks and delamination started to appeared and propagated rapidly leading to the load decreased sharply with displacement increasing. The ultimate failure occurred when the displacement increased to 1.50 mm for junction specimen *J1*, 2.53 mm for junction specimen *J2* and 2.45 mm for junction specimen *J3* at corresponding load level of 2.04kN for junction specimen *J1*, 2.79kN for junction specimen *J2* and 5.55kN for junction specimen *J3*. Results obtained from both the trilinear and bilinear models for different joints group are presented in Fig. 13. The linear stiffness, K_l, for *J1, J2* and *J3* junction specimens is 6.59kN/mm, 5.74kN/mm and 6.53kN/mm, respectively, while the average linear stiffness, K_m, for *J1, J2* and *J3* junction specimens is 4.76kN/mm, 4.83kN/mm and 5.96kN/mm, respectively. Results obtained from both the trilinear and bilinear models agreed well with the experimental results, however, results of the bilinear model of junction *J1,* at both stages as well as the analytical results of junctions *J2* and *J3* at the descending stage are

relatively on the conservative side.

As shown in Figure (14-a), failure mode for junction *J1* is in the form of the development of through-the-thickness inclined crack at the junction's resin rich zone. For WFJ specimen *J2*, inclined cracks near the start of the fillet zone and delamination of the fillet zone that were developed at the opposite side where the inclined cracks were observed led to the failure of this junction as shown in Figure (14-b). The failure mode of junction *J3* was initiated by the development of presents parallel cracks near the fillet starting position followed by delamination at both sides of the fillet zone (refer to Figure 14-c). Due to the fact that junctions J2 and *J3* have larger fillet radii and smaller web thickness, as compared to junction specimen J1, no cracks were developed at the WFJ's resin-rich zone.

3.2 Experimental Results of Adhesively-bonded Joints Group: Summaries of experimental results of the different adhesively-bonded joints group evaluated in this study are listed in Tables (8), (9) and (10). Figure (15) presents axial load versus axial displacement curves for all adhesive joints group. Figure (16) illustrates the different failure modes of adhesively-bonded joints group assessed in this study.

As shown in these figures, axial displacement increased linearly as the load increased up to an average displacement of 1.76 mm for bonded joint *AJ1*, 1.64 mm for *AJ2* and 1.37 mm of *AJ3* that occurred at associated load levels of 5.67kN, 12.28kN and 10.76kN, respectively. It is noted that the initial load-displacement slop of bonded joint AJ3 relatively scattered compared with bonded joint *AJ1* and *AJ2.* Beyond these loading levels, stiffness degradations were observed and the load-displacement curves behaved nonlinearly until reaching average axial

displacements of 2.37 mm for specimen *AJ1*, 2.80 mm for specimen *AJ2* and 2.40 mm for specimen *AJ3* with associated loads of 6.87 kN for specimen *AJ1*, 10.26kN for specimen *AJ2* and 16.04kN for specimen *AJ3*. It is noted that the load-displacement curves of specimen *AJ2* decreased after linear range point (P_l, d_l) and the stage from linear range point (P_l, d_l) to the nominal peak load point (P_f, d_f) is much long. Local cracks and delamination started to appeared and rapidly propagate beyond these loading levels leading to appreciable drop in strength accompanied with increase of resulting axial displacements shown in Figure (15). The ultimate failure occurred when axial displacement approached 7.43 mm for specimen *AJ1*, 5.38 mm for specimen *AJ2* and 3.15 mm for specimen at corresponding load levels of 2.81kN for specimen *AJ1*, 1.88kN for specimen *AJ2* and 5.73kN for specimen *AJ3*.

Results obtained from both the trilinear and bilinear models for different bonded joints groups are presented in Figure (15). The linear stiffness K_l of bonded specimens *AJ1, AJ2* and *AJ3* are 3.24kN/mm, 7.49kN/mm and 7.83 kN/mm, respectively, while the average linear stiffness K_m of *AJ1, AJ2* and *AJ3* are 2.76kN/mm, 3.21kN/mm and 7.30kN/mm, respectively.

The trilinear and bilinear model agreed well with the experimental results except that the results obtained from the trilinear model of *AJ2* at the second stage where the predicated values are larger than. In addition, one can notice that the predicated results obtained from the bilinear model for bonded specimen *AJ2* are relatively conservative as compared to corresponding experimental results.

As is shown in Figure (16-a), an inclined crack appeared throughout the resin rich zone of *AJ1-1* and delamination of the fillet position of *AJ1-1* also occurred leading to the failure of *AJ1*.

As is shown in Figure (16-b), *AJ2* suffered from inclined crack that were initiated near the fillet end of specimen *AJ2-2*. As is shown in Figure (16-c), the typical failure of bonded-specimen *AJ3* group was initiated by the development of inclined cracks at the arc starting position (specimen *AJ3-1)* or at the middle of the fillet (specimen *AJ3-1*). No visual cracks or debonding were detected at the adhesive layer.

3.3 Experimental Results Discussion

3.3.1 Experimental results summary

A comparison between the axial load capacity (P_l, P_m, P_f, P_u) and stiffness (K_l, K_m) of the six web-flange junction specimens are presented Figure (17) in the form of a bar chart. As one can see, the axial tensile load capacity and axial tensile stiffness of specimen *AJ3* is the largest except P_l among all specimens, the axial tensile load capacity and axial tensile stiffness of specimen *J3* is largest among "*J*" group and the axial tensile load capacity and axial tensile stiffness of specimen *AJ3* is largest except that axial load P_l of *AJ2* is largest among "*AJ*" group.

3.3.2 Web thickness effects

Web thickness effects on axial tensile load capacity and axial tensile stiffness of the web-flange junction specimens present in Fig. 18. The web thickness increased from 6 mm to 12.5 mm for specimen *J1* and *AJ1*, from 4.5 mm to 12.5 mm for specimen *J2* and *AJ2*, specimen *J3* and *AJ3*. Experimental results indicated that the axial tensile load capacity of "*AJ-#*" group was slightly larger than "J-#" group except P_u and P_f of *J2-AJ2* specimens while the axial tensile stiffness K_m of "J-#" group was larger than "*AJ-#*" group, the axial tensile stiffness K_l of "J-#" group was less than "*AJ-#*" group except of "*J1*" specimen, indicating that larger web thickness may

slightly increase the axial load capacity but have no obvious effect on axial tensile stiffness. It is also noted that the larger web thickness ratio (see Fig. 18) did not lead to a larger axial force ratio, indicating that the axial tensile load does not increase proportionally as the web thickness increases.

3.3.3 Flange thickness effects

Flange thickness effects on axial tensile load capacity and axial tensile stiffness of the web-flange junction specimens present in Fig. 19. The flange thickness increased from 6mm to 8mm for specimen *J2* and *J3*, specimen *AJ2* and *AJ3*. Experimental results showed that the axial tensile load capacity of "#-3" group was larger than "#-2" group except P_l of *AJ2-AJ3* group and the axial tensile stiffness of "#-3" group was also larger than "#-2" group, indicating the larger flange thickness leads to larger axial tensile load capacity and axial stiffness. However, with same flange thickness ratio increment of each group, the axial tensile force ratio and axial tensile stiffness ratio increment of each group (see Fig. 19) is quite different.

3.3.4 Fillet radius effects

Fillet radius effects on axial strength and axial stiffness of the web-flange junction specimens present in Fig. 20. The fillet radius increased from 10 mm to 20 mm for specimen *J1* and specimen *J2* and increased from 10 mm to 30 mm for specimen *AJ1* and specimen *AJ2*. The axial tensile load capacity of "#-1" group was less than "#-2" group except P_u of *AJ1-AJ2* group, the axial stiffness K_l of specimen *J1* was less than that of specimen *J2, however,* the axial stiffness K_m of specimen *J1* is similar to that of specimen *J2*. *Also,* the axial stiffness of specimen *AJ1* was less than that of specimen *AJ2*, indicating that the increasing fillet radius

may increase the axial load capacity, however, this increase has no obvious effect on the junction axial tensile stiffness. In addition, it was found that larger fillet radius ratio do not contribute an increase in axial tensile capacity of the junction.

3.3.5 Axial load capacity and axial stiffness interaction

The relationship of axial tensile load capacity and axial tensile stiffness is illustrated in Fig. 21. From this figure, one can see that larger axial tensile stiffness did not guarantee higher junction's axial tensile load capacity (*specimens J1 in Fig. 21-a, specimens J1 and AJ2 in Fig. 21-b and specimens J1, J3 and AJ2 specimens in Fig. 21-c*).

In summary, results indicated that the larger web thickness may slightly increase the axial load capacity but does not have an obvious effect on the junction's axial tensile stiffness. Also, it is concluded that the larger flange thickness leads to larger axial tensile load capacity and axial stiffness and that the increasing fillet radius may increase the axial load capacity but have no obvious effect on axial tensile stiffness. However, these conclusions are different from published research on composite T-joints behavior for aerospace applications where increasing web and flange thicknesses and fillet radius do not proportionally guarantee an increase in the axial tensile load capacity and stiffness of web-flange junctions due to reasons described earlier in this paper. Figure 22 shows a typical differences between composites used in construction (Fig. 22-b) and those commonly used for aerospace and military applications (Fig. 22-a). Much attention should be paid on the fabric fold effects in the simulation based on classical laminate theory.

4. EXPERIMENTAL RESULTS AFTER HYGROTHERMAL AGING

4.1 Experimental results

Table 11 and 12 depict the changes in axial ultimate capacity of *J1* junction specimen, at six hygrothermal aging environments, as a function of time. The largest reduction in the WFJ's axial ultimate capacity immersed in water environments are: 18.3% (4.62 kN), 22.7% (4.37 kN) and 25.1% (4. 23 kN) at the temperatures of 40℃, 60℃ and 80℃ respectively at the end of hygrothermal aging. Also, the largest reduction in axial ultimate capacity of the WFJ specimen that was immersed in artificial seawater environments are 18.2% (4.62 kN) , 19.37% (4.55 kN) and 24.0% (4. 29kN) at the temperature of 40℃, 60℃ and 80℃ respectively at the end of hygrothermal aging.

Axial experiment failure modes comparison before and after hygrothermal aging were shown in Fig. 23. It indicates that cracks size and width throughout the resin-rich (or matrix-dominated) zones have increased after certain time exposure and aging. The colors of specimens gradually turned from green to yellow after long-term hygrothermal aging.

4.2 Results discussion

4.2.1 Hygrothermal environment effects

Hygrothermal environment effects on ultimate axial force P_f along time variation presents in Fig. 24. It is noted that the axial ultimate force present increasing trend from 0 hours to 672 hours and decreased later at temperatures of 40℃and 60℃ exposed both in water environment and artificial seawater environment. The experimental results show that the ultimate axial force retention reduction difference between water environments and artificial seawater environments at temperatures of 40℃and 60℃ is relatively small but the ultimate axial force

in the water environments degraded more seriously than in artificial seawater environments at a temperature of 80℃.

4.2.2 Temperature effects

Temperature effects on ultimate axial force retention along time variation present in Fig. 25. Experimental results showed that the ultimate axial force retention reduction is larger at higher temperatures in water environment. Experimental results also showed that the difference of the ultimate axial force retention reduction at different temperatures is relatively small from 0.0 hours to 672.0 hours and is larger at higher temperatures from 672.0 hours to 4,392.0 hours in artificial seawater environment.

5. CONCLUSIONS & RECOMMENDATIONS

This paper presents a summary of results of a pioneering multi-phase experimental study that was performed on six different web-flange junctions and bonded joints in order to investigate the as-built (unexposed) axial characteristics of such joints. In addition, one of the web-flange junctions group was exposed to both freshwater and artificial seawater environments at different temperatures including 40℃, 60℃and 80℃, to assess the hygrothermal effects on axial characteristics of junctions and bonded joints.

(1) The experimental data on axial tensile load capacity and stiffness of six different web-flange junctions obtained from this study could provide a basis for establishing design limit-state basis for PFRP structures that considered behavior of web-flange junction strength and stiffness limitations [28]. Experimental results indicated that the axial tensile load capacity and stiffness of specimen *AJ3* is the largest among all specimens evaluated in this study except for

the P_l value. It was also shown that the axial tensile load capacity and stiffness of specimen *J3* is the largest among the "*J*" group. Also, the axial tensile load capacity and stiffness of specimen *AJ3* is the largest among "*AJ*" group, except for the value of axial load P_l which has the highest value corrospending to adhesively-bonded specimen *AJ2*.

(2) Results of this study also indicated that the larger web thickness may slightly increase the axial load capacity; however, it has little effect on the junction axial tensile stiffness. Also, results indicated that the larger flange thickness leads to larger axial tensile load capacity and stiffness and that the larger fillet radius may increase the axial load capacity with a minor effect on the junction's axial tensile stiffness. Based on the findings gathered from this study and in contrary to published work in this area related to the behavior T-joints in aerospace applications, it was found that increasing the web and flange thicknesses as well as the fillet radius do not proportionally guarantee an increase in the axial tensile load capacity and stiffness of pultruded web-flange junctions due to fabric fold effects and other fabrication related issues. For this reason, much attention should be paid in simulating the behavior of WFJs that must include the fabric fold effects.

(3) Several interrelated failure modes were identified from the results of this study that were mainly initiated at the junction/joint locations. For example, failure mode of WFJ specimen *J1* was in the form of growth and propagation of through-the-thickness inclined cracks at the junction's internal resin-rich zone. Similar inclined cracks were also a major contributor to the ultimate failure of junction specimen *J2,* however, the location of such cracks in this case were initiated near the stating zone of the fillet, at both sides, leading to delamination of the

junction area For WFJ specimen *J3,* failure was initiated when near-the-fillet parallel cracks appeared on the both side of the junction surface. Similar failure pattern was detected for specimen *AJ1-1* in the form of the development of through-the-thickness at resin-rich zone inclined crack followed by local delamination of the fillet. Similar cracks were observed near the end of the fillet of specimen *AJ2-2.* The failure of specimen of specimen *AJ3* was in the form of the initiation and propagation of inclined cracks at the fillet zone. No cracks or delamination appeared in the adhesive bond line.

(4)The reduction in the WFJ's axial ultimate capacity immersed in water environments are: 18.3% (4622.5N), 22.7% (4366.0N) and 25.1% (4231.5N) at the temperatures of 40℃, 60℃ and 80℃ respectively at the end of hygrothermal aging. Also, the reduction in axial ultimate capacity of the WFJ specimen that was immersed in artificial seawater environments are 18.2% (4620.0 N) , 19.37% (4552.3 N) and 24.0% (4289.3 N) at the temperature of 40℃, 60℃ and 80℃ respectively at the end of hygrothermal aging.

(5) It is noted that the axial ultimate force present increasing trend from 0 hours to 672 hours and decreased later at temperatures of 40℃and 60℃ exposed both in water environment and artificial seawater environment. The experimental results show that the ultimate axial force retention reduction difference between water environments and artificial seawater environments at temperatures of 40℃and 60℃ is relatively small but the ultimate axial force in the water environments degraded more seriously than in artificial seawater environments at a temperature of 80℃. Experimental results showed that the ultimate axial force retention reduction is larger at higher temperatures in water environment. Experimental results also

showed that the difference of the ultimate axial force retention reduction at different temperatures is relatively small from 0.0 hours to 672.0 hours and is larger at higher temperatures from 672.0 hours to 4,392.0 hours in artificial seawater environment.

(6) Results of this part of the multiphase investigation highlighted the sensitivity of pultrude composites to hygrothermal environment, especially at the critical web/flange junction of common bridge structural profiles. In addition, results explained the reason behind some recent failures of pultruded decks that were witnessed by the second author. The impact of such environment on axial stiffness of WFJs was also identified that affect the structural integrity of pultruded deck systems especially when local buckling and repeated loading exist. It is clear that there is an urgent proactive reaction from the pultrusion industry and the engineering community to understand the criticality of this inherent deficiency and provide immediate remedy for such major issue. This can done in two ways; (i) redesigning the WFJ resin -rich- or matrix-dominated zone by adding special reinforcements and ensuring continuity of fibers between flanges and the web, (ii) as an immediate resolution, open web-section should be stiffened with proper external details and flanges should supported continuously to avoid such damage such as the multidirectional Universal Connector developed by the second author [49] or any other proper stiffeners. As mentioned earlier the ASCE MOP102 [8] contains recommendations for remediating such deficiency.

ACKNOWLEDGEMENTS

This work was supported by the National Natural Science Foundation [Grant # 51578406] of People's Republic of China. The principal author acknowledges the financial support provided

by the China Scholarship Council (CSC) [Grant # 201506260100].

REFERENCES

[1] Mosallam, AS. Chapter 45: Composites in Construction, Materials Selection Handbook, John Wiley Publishing Co., edt. Kuitz, January 2002, pp.1369-1422.

[2] Bank LC. Composites for Construction: structural design with FRP materials: John Wiley & Sons; 2006.

[3] Mosallam, AS; Bayraktar, A; Elmikawi, M; Pul, S; Adanur, S "Polymer composites in construction: an overview." SOJ Materials Science & Engineering (Open Access), 2015, 2(1), 25.

[4] Mosallam, A., & Banerjee, S. (2011). Enhancement in in-plane shear capacity of unreinforced masonry (URM) walls strengthened with fiber reinforced polymer composites. Composites Part B: Engineering, 42(6), 1657-1670.

[5] Kim, J. J., Noh, H. C., Taha, M. M. R., & Mosallam, A. (2013). Design limits for RC slabs strengthened with hybrid FRP–HPC retrofit system. Composites Part B: Engineering, 51, 19-27.

[6] Mosallam, A. S. (2016). Structural evaluation and design procedure for wood beams repaired and retrofitted with FRP laminates and honeycomb sandwich panels. Composites Part B: Engineering, 87, 196-213.

[7] Feo, Luciano, Ayman S. Mosallam, and Rosa Penna. (2013) "Mechanical behavior of web–flange junctions of thin-walled pultruded I-profiles: An experimental and numerical

evaluation." Composites Part B: Engineering 48: 18-39.

[8] Mosallam, A. S. Design guide for FRP composite connections, ASCE manuals and reports on engineering practice MOP (102), American Society of Civil Engineers (ASCE), Reston, Virginia, USA, 2011, ISBN 978-0-7844-0612-0

[9] Hai, N. D., Mutsuyoshi, H., Asamoto, S., & Matsui, T. Structural behavior of hybrid FRP composite I-beam. Construction and Building Materials, 2010, 24(6), 956-969.

[10] Restrepo, E., Cousins, T., & Lesko, J. (2005). Determination of bridge design parameters through field evaluation of the Route 601 Bridge utilizing fiber-reinforced polymer girders. Journal of Performance of Constructed Facilities, 19(1), 17-27.

[11] Hayes, M. D., Lesko, J. J., Haramis, J., Cousins, T. E., Gomez, J., & Masarelli, P. Laboratory and field testing of composite bridge superstructure. Journal of Composites for Construction, 4(3), 120-128, 2000.

[12] Nordin, H., & Täljsten, B. (2004). Testing of hybrid FRP composite beams in bending. Composites Part B: Engineering, 35(1), 27-33.

[13] Deskovic, N., Triantafillou, T. C., & Meier, U. (1995). Innovative design of FRP combined with concrete: short-term behavior. Journal of Structural Engineering, 121(7), 1069-1078.

[14] He, J., Liu, Y., Chen, A., & Dai, L. Experimental investigation of movable hybrid GFRP and concrete bridge deck. Construction and Building Materials. 2012, 26(1): 49-64.

[15] Xin, H., Liu, Y., He, J., Fan, H., & Zhang, Y. (2015). Fatigue behavior of hybrid GFRP-concrete bridge decks under sagging moment. Steel and Composite Structures, 18, 925-946.

[16] Xin, H., Liu, Y., & Du, A. Thermal analysis on composite girder with hybrid GFRP-

concrete deck. Steel and Composite Structures. 2015, 19(5): 1221-1236.

[17] Keller, T., Rothe, J., De Castro, J., & Osei-Antwi, M. (2013). GFRP-balsa sandwich bridge deck: Concept, design, and experimental validation. Journal of Composites for Construction, 18(2), 04013043.

[18] Satasivam S, Bai Y, Zhao XL. Adhesively bonded modular GFRP web-flange sandwich for building floor construction. Composite Structures, 2014, 111: 381-392.

[19] Mosallam, A. S., & Bank, L. C. (1992). Short-term behavior of pultruded fiber-reinforced plastic frame. Journal of Structural Engineering, 118(7), 1937-1954.

[20] Mosallam, A. S. (1995). Connection and reinforcement design details for pultruded fiber reinforced plastic (PFRP) composite structures. Journal of reinforced plastics and composites, 14(7), 752-784.

[21] Mosallam, A. S., Feo, L., Elsadek, A., Pul, S., & Penna, R. (2014). Structural evaluation of axial and rotational flexibility and strength of web–flange junctions of open-web pultruded composites. Composites Part B: Engineering, 66, 311-327.

[22] Bank, Lawrence C., and Jianshen Yin. "Failure of web-flange junction in postbuckled pultruded I-beams." Journal of Composites for Construction. (1999): 177-184.

[23] Bank, L. C., Nadipelli, M., & Gentry, T. R. (1994). Local buckling and failure of pultruded fiber-reinforced plastic beams. Journal of engineering materials and technology, 116(2), 233-237.

[24] Ascione, F., & Mancusi, G. (2013). The influence of the web-flange junction stiffness on the mechanical behavior of thin-walled pultruded beams. Composites Part B: Engineering, *55*,

599-606.

[25] Turvey G J, Zhang Y. Shear failure strength of web–flange junctions in pultruded GRP WF profiles [J]. Construction and Building Materials, 2006, 20(1): 81-89.

[26] Turvey, G. J., & Zhang, Y. (2006). Characterisation of the rotational stiffness and strength of web-flange junctions of pultruded GRP WF-sections via web bending tests. Composites Part A: Applied Science and Manufacturing, 37(2), 152-164.

[27] Turvey, G. J., & Zhang, Y. (2005). Tearing failure of web–flange junctions in pultruded GRP profiles. Composites Part A: Applied Science and Manufacturing, 36(2), 309-317.

[28] Ascione, F., Feo, L., Lamberti, M., Minghini, F., & Tullini, N. (2016). A closed-form equation for the local buckling moment of pultruded FRP I-beams in major-axis bending. Composites Part B: Engineering, 97, 292-299.

[29] A.S. Mosallam. “Durability of Pultruded Fiber Reinforced Polymer (PFRP) Composites in Mining Environments,” in Durability of Fiber Reinforced Polymer (FRP) Composites for Construction, Edts. B. Benmokrane and H. Rahman, 1998, ISBN: 0-921303-88-2, pp. 649-659.

[30] Dutta, P.K., Mosallam, A.S. and R. Lampo. Response of FRP Composite Joints in Hygrothermal Environments, Proceedings, ICPCM - A New Era of Building, Cairo, EGYPT, Feb. 18-20, (2003).

[31] Liao, K., Schultheisz, C. R., & Hunston, D. L. (1999). Effects of environmental aging on the properties of pultruded GFRP. Composites Part B: Engineering.:30(5), 485-493.

[32] Liao, Kin, Carl R. Schultheisz, and Donald L. Hunston. Long-term environmental fatigue of pultruded glass-fiber-reinforced composites under flexural loading. International Journal of

Fatigue 21.5 (1999): 485-495.

[33] Iqbal, Mohammed Asif, Fatigue Life of Pultruded and Hand Lay-Up GFRP Exposed to Different Environmental Conditions, (2002). Ph.D. Thesis, University of Maine, USA, 175p.

[34] Correia, J. R., Cabral-Fonseca, S., Branco, F. A., Ferreira, J. G., Eusébio, M. I., & Rodrigues, M. P. Durability of pultruded glass-fiber-reinforced polyester profiles for structural applications. Mechanics of Composite Materials. 2006: 42(4), 325-338.

[35] Abanilla, M. A., Li, Y., & Karbhari, V. M. Durability characterization of wet layup graphite/epoxy composites used in external strengthening. Composites Part B: Engineering, 2006:37(2), 200-212.

[36] Karbhari, V. M., & Abanilla, M. A. Design factors, reliability, and durability prediction of wet layup carbon/epoxy used in external strengthening. Composites Part B: Engineering, 2007:38(1), 10-23.

[37] Xin H, Liu Y, Mosallam A, Zhang Y, (2016). Moisture diffusion and hygrothermal aging of pultruded glass fiber reinforced polymer laminates in bridge application, Composites Part B, 100: 197-207.

[38] Pour-Ghaz, M., Miller, B. L., Alla, O. K., & Rizkalla, S. (2016). Do mechanical and environmental loading have a synergistic effect on the degradation of pultruded glass fiber reinforced polymers?. Composites Part B: Engineering.

[39] Bazli, M., Ashrafi, H., & Oskouei, A. V. (2016). Effect of harsh environments on mechanical properties of GFRP pultruded profiles. Composites Part B: Engineering, pp.203-215.

[40] Kafodya, I., Xian, G., & Li, H. (2015). Durability study of pultruded CFRP plates

immersed in water and seawater under sustained bending: Water uptake and effects on the mechanical properties. *Composites Part B: Engineering*, *70*, 138-148.

[41] Heshmati, M., Haghani, R., & Al-Emrani, M. (2016). Effects of moisture on the long-term performance of adhesively bonded FRP/steel joints used in bridges. Composites Part B: Engineering, 92, 447-462.

[42] Bank LC, Gentry TR, Barkatt A. Accelerated test methods to determine the long-term behavior of FRP composite structures: environmental effects. Journal of Reinforced Plastics and Composites. 1995; 14(6):559-87.

[43] Mouzakis DE, Zoga H, Galiotis C. (2008). Accelerated environmental ageing study of polyester/glass fiber reinforced composites (GFRPCs). Composites part B: Engineering, 39(3):467-75.

[44] ISO, B. 527-4. Plastics–determination of tensile properties–part 4: test conditions for isotropic and orthotropic fibre-reinforced plastic composites. International Organization for Standardization (ISO), Geneva, Switzerland, 1997.

[45] ISO, B. 604. Plastics–determination of compressive properties. International Organization for Standardization (ISO), Geneva, Switzerland, 2002.

[46] ISO, B. 14129. Fibre-reinforced plastic composites– Determination of the in-plane shear stress/shear strain response, including the in-plane shear modulus and strength, by the±45 tension test method. International Organization for Standardization (ISO), Geneva, Switzerland, 1997.

[47] ISO, B. 14125. Fiber-reinforced plastic composites -- Determination of flexural properties. International Organization for Standardization (ISO), Geneva, Switzerland, 1998.

[48] ISO, B. 14130. Fibre-reinforced plastic composites–Determination of apparent interlaminar shear strength by short-beam method, International Organization for Standardization (ISO), Geneva, Switzerland, 1998.

[49] Mosallam, A.S., Bedewi, N.E. and E. Goldstein (1994). "Optimization and Design Analysis of FRP Universal Connector," Polymer and Polymer Composites, 2(2), pp.115A-123A.

LIST OF FIGURES

Figure (1): Difference in Quality and Accuracy of Stacking Sequence of Composite Laminates: (a) Pultruded Composites, (*Classical Lamination Theory is Improper*) (b) High-quality Laminated Composites (*Classical Lamination Theory Applies*),

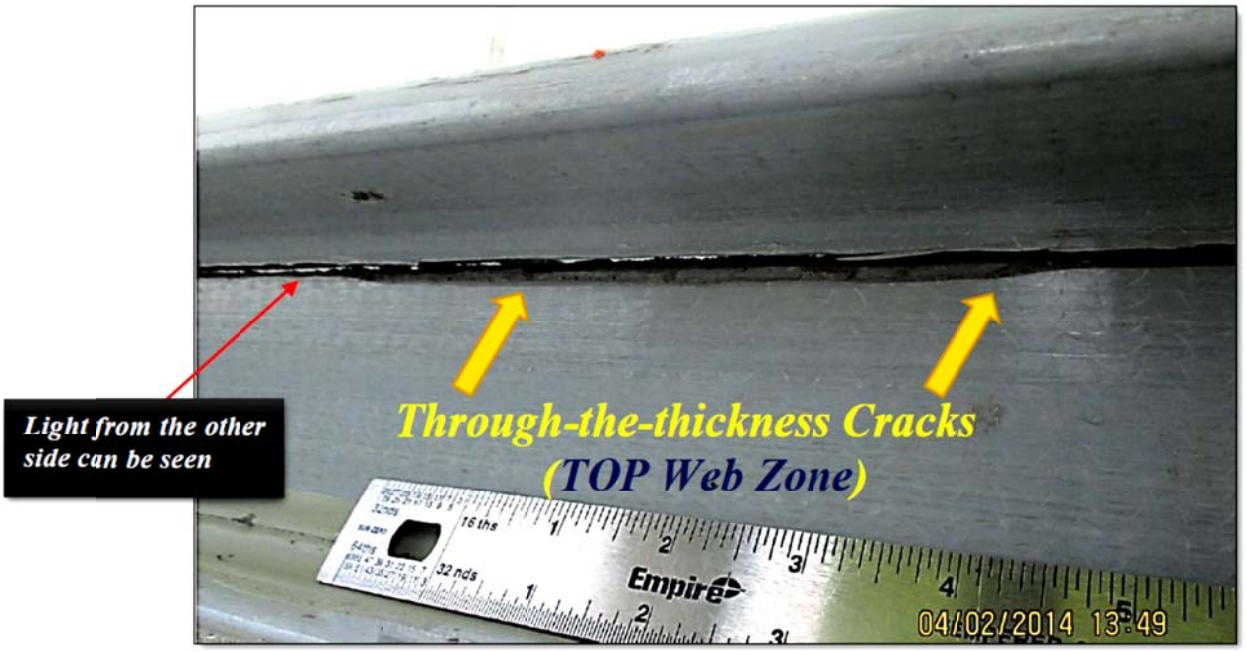

Figure (2): Web/Flange Failure of a Pultruded Composites Bridge Deck in USA

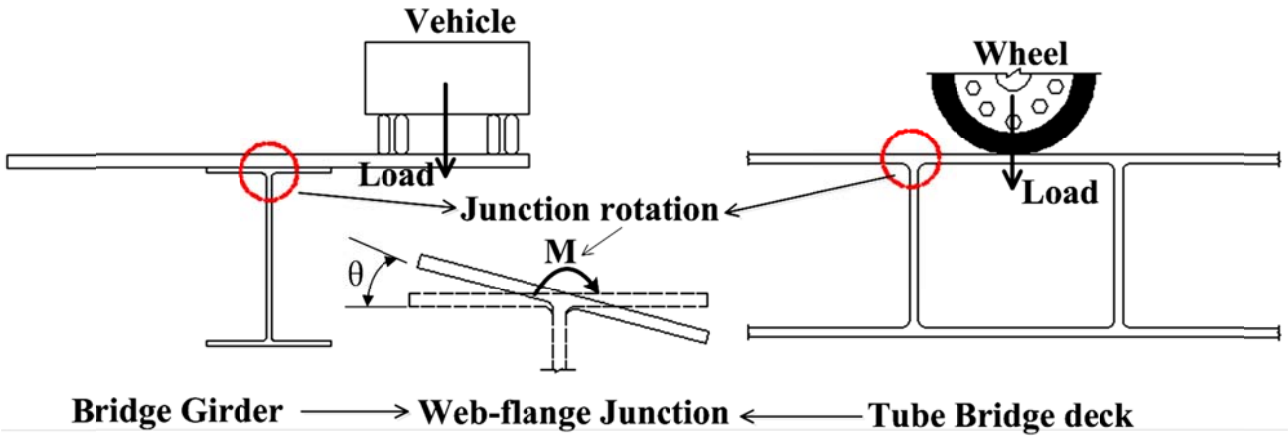

Figure (3): Rotation moments of web-flange junctions in a typical bridge deck

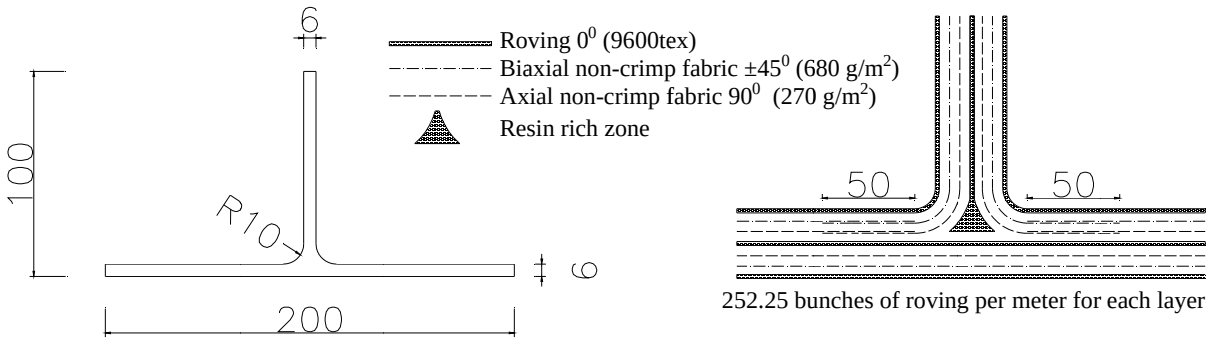

252.25 bunches of roving per meter for each layer

(a) Specimen *J1*

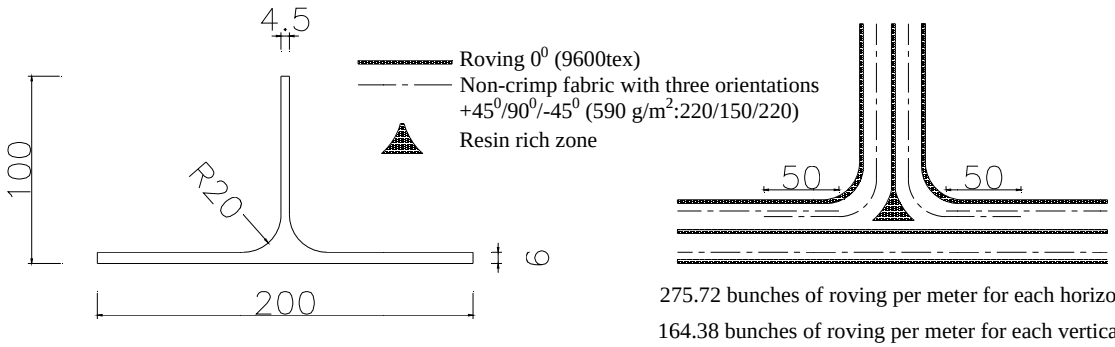

275.72 bunches of roving per meter for each horizontal layer

164.38 bunches of roving per meter for each vertical layer

(b) Specimen *J2*

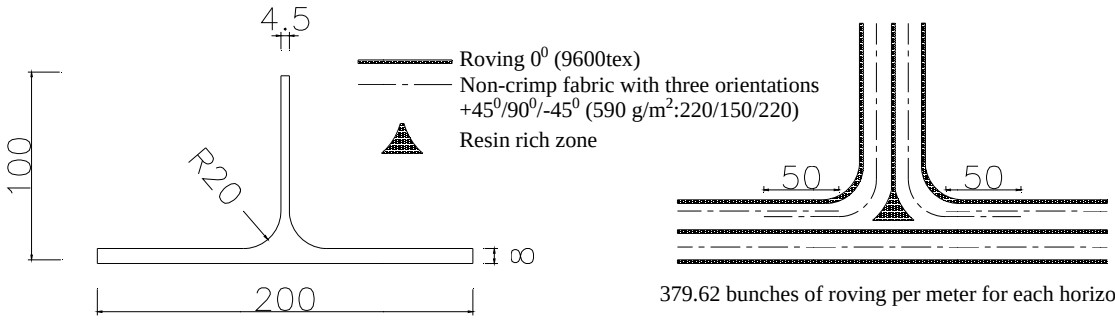

379.62 bunches of roving per meter for each horizontal layer

164.38 bunches of roving per meter for each vertical layer

(c) Specimen *J3*

Figure (4): Cross section and laminates' lay-up of junctions (*Units: mm*)

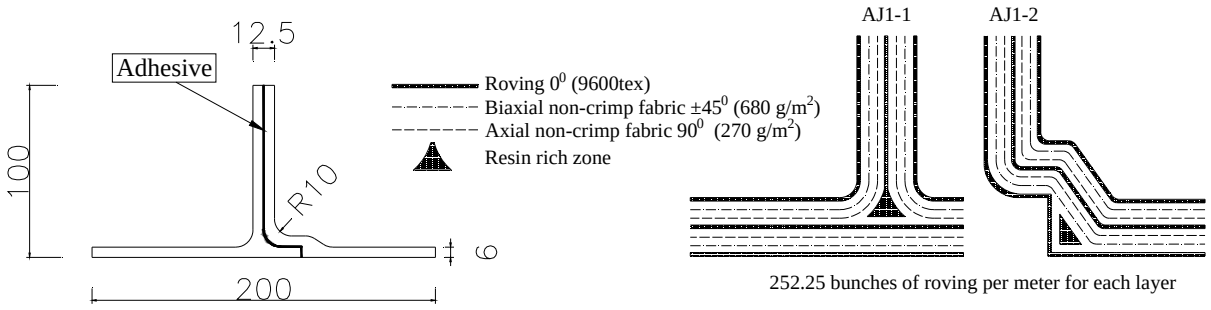

(a) Specimen *AJ1*

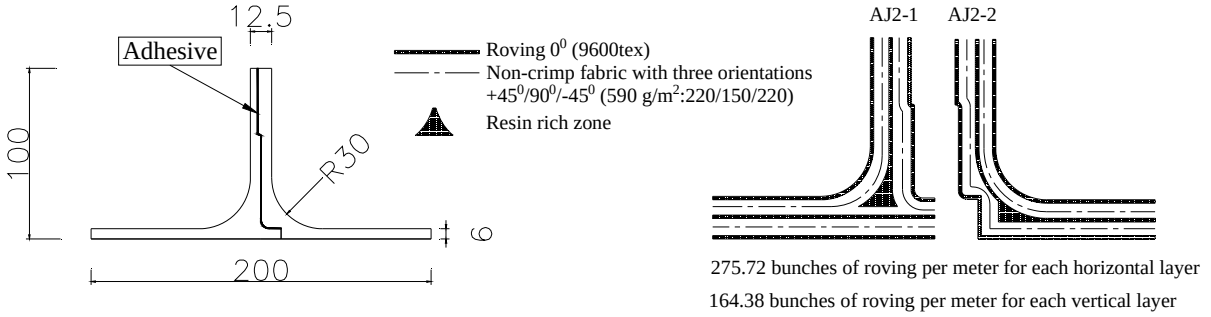

(b) Specimen *AJ2*

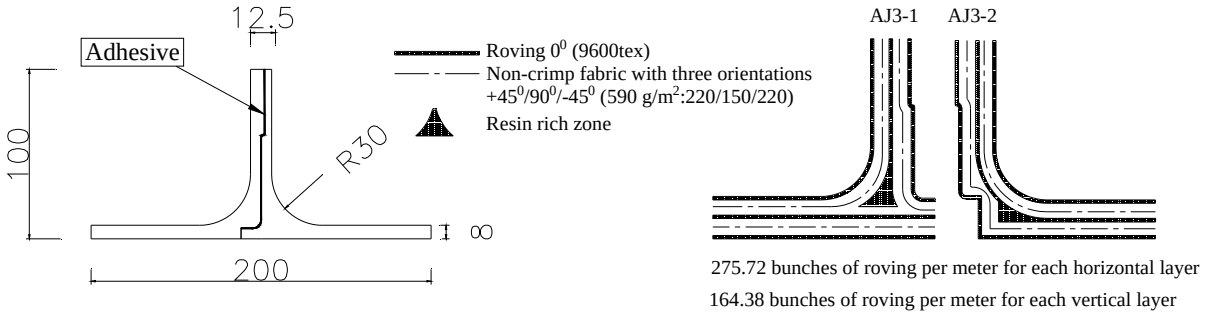

(c) Specimen *AJ3*

Figure (5): Cross section and laminates' lay-up of adhesive junctions (*Units: mm*)

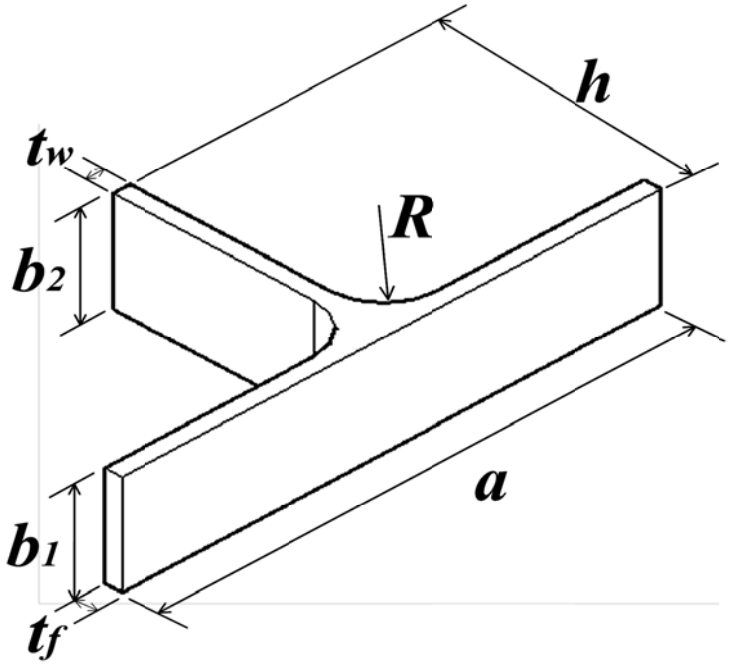

Figure (6): Schematic of a typical pultruded web-flange junction

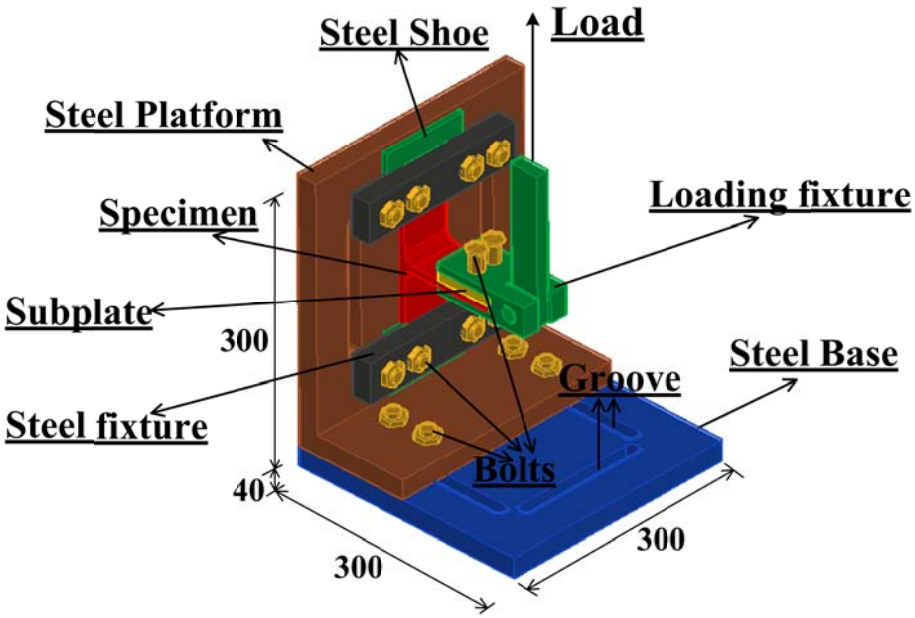

Figure (7): Typical Test setup (*Units: mm*)

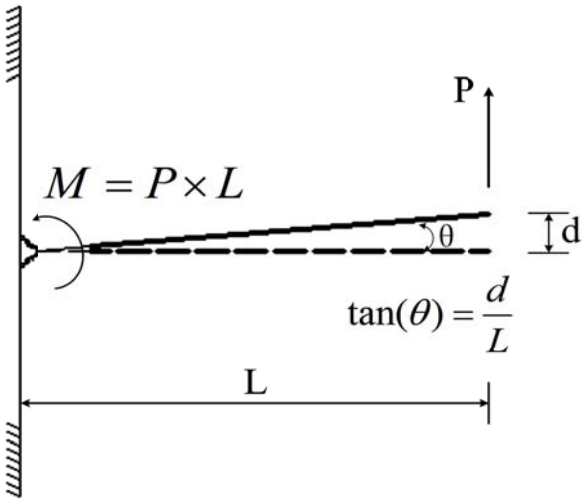

Figure (8): Structural model of web-flange junction experimental setup

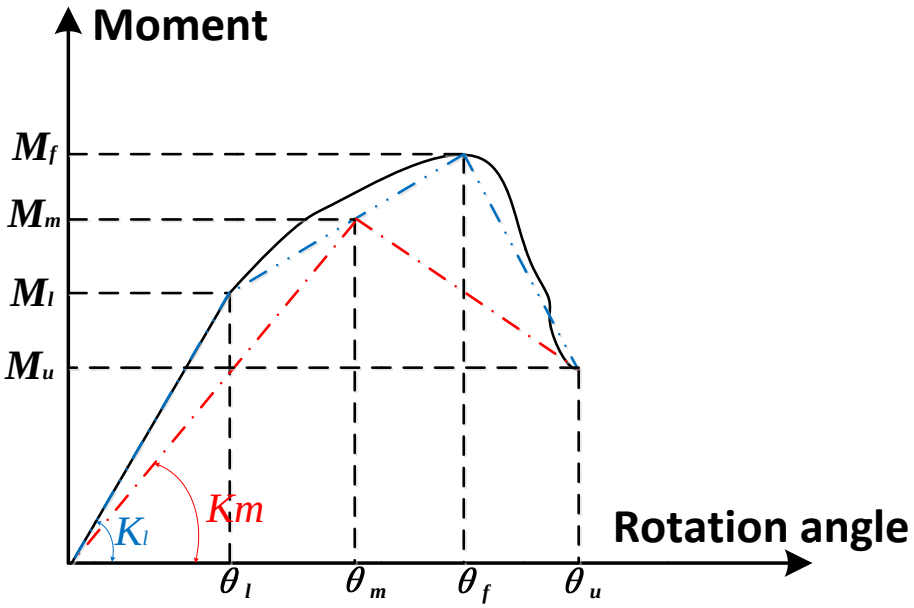

Figure (9): Schematic of trilinear and bilinear models

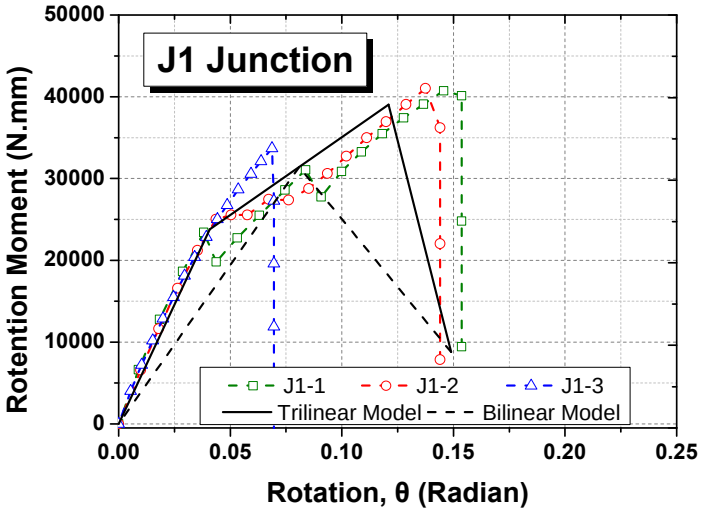

(a) Specimen J1

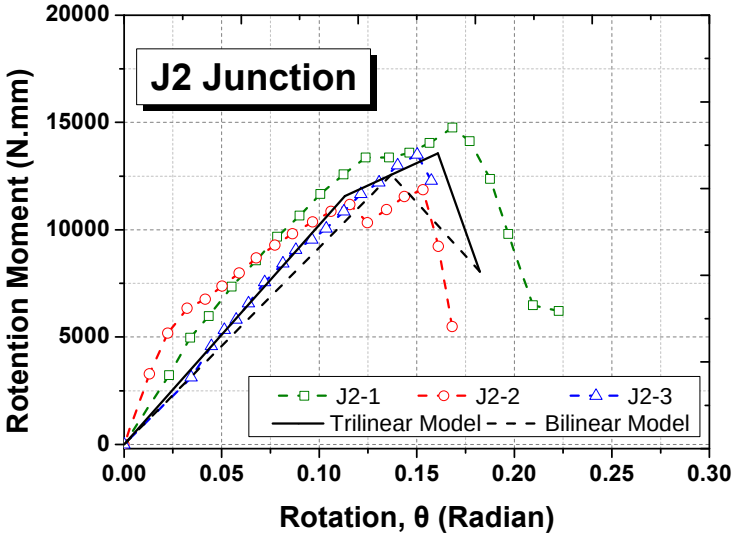

(b) Specimen J2

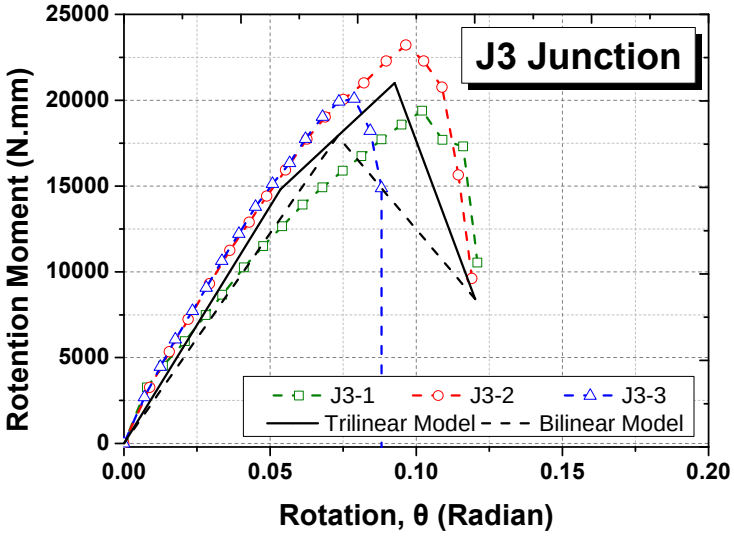

(c) Specimen J3

Figure (10): Applied moment versus rotational angle for different junction group

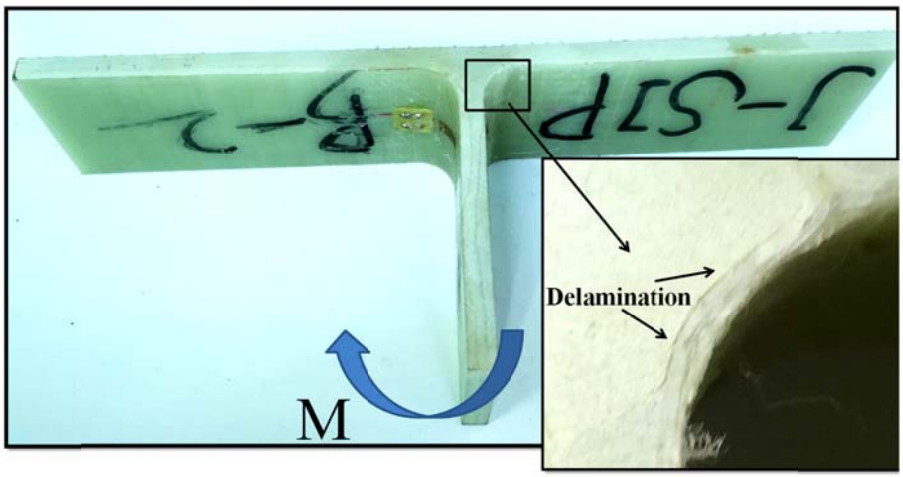

(a) Specimen J1

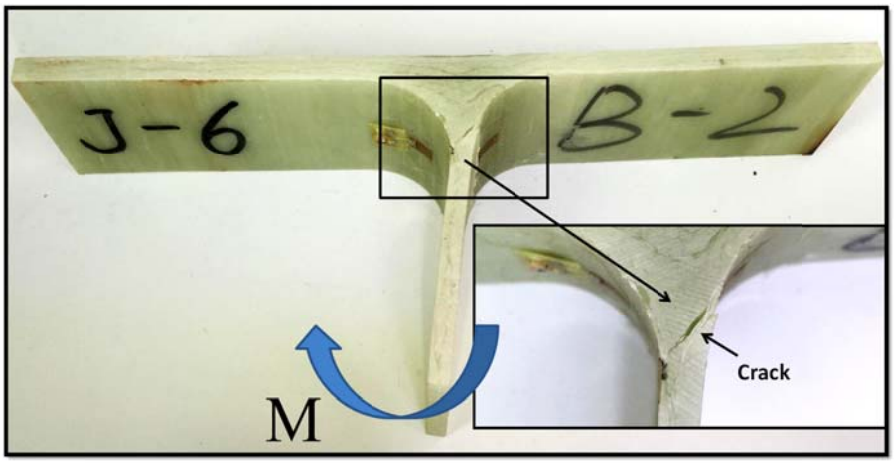

(b) Specimen J2

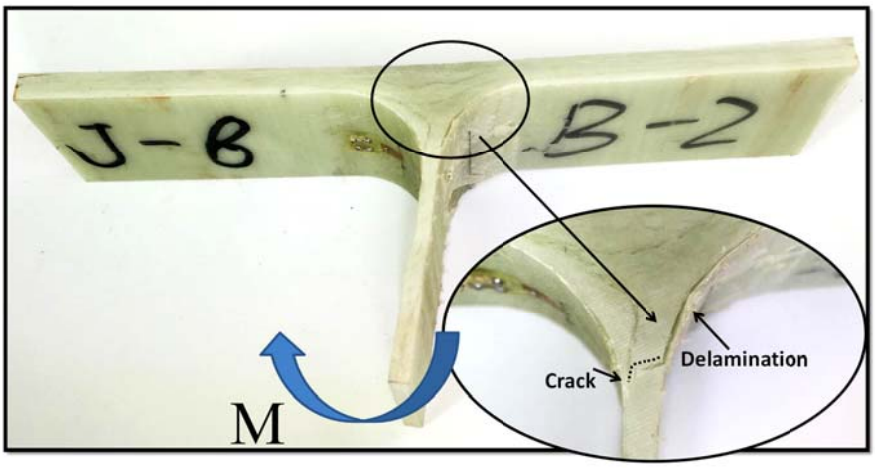

(c) Specimen J3

Figure (11): Failure modes of junctions group

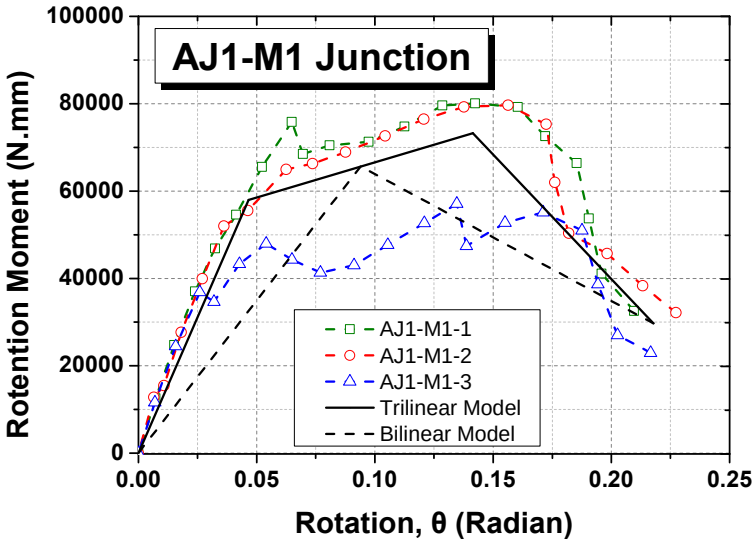

(a) Specimen *AJ1-M1*

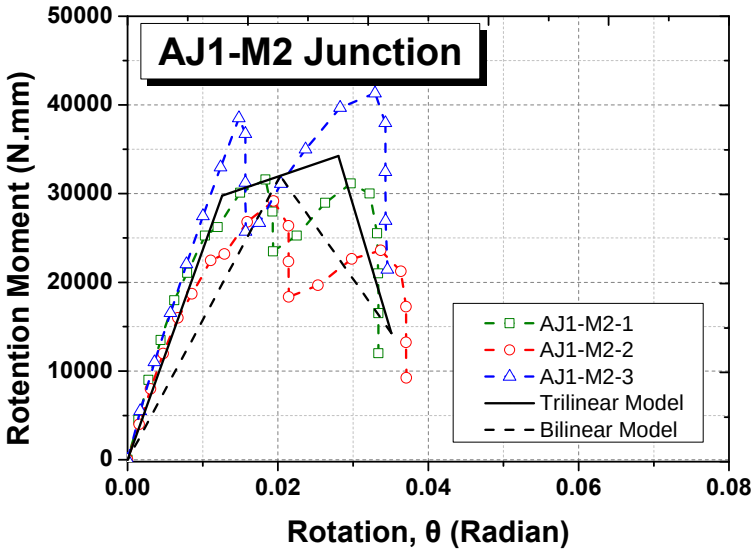

(b) Specimen *AJ1-M2*

Figure (12): Applied moment versus rotational angle of specimen *AJ1*

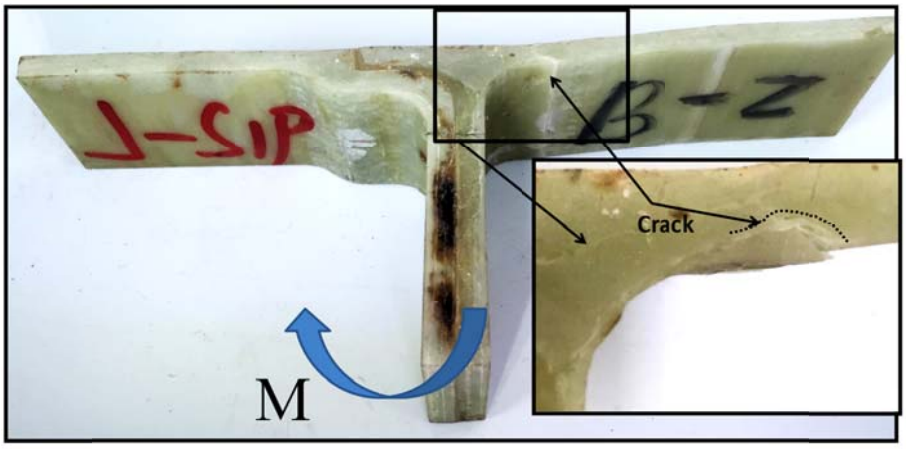

(a) Specimen *AJ1-M1*

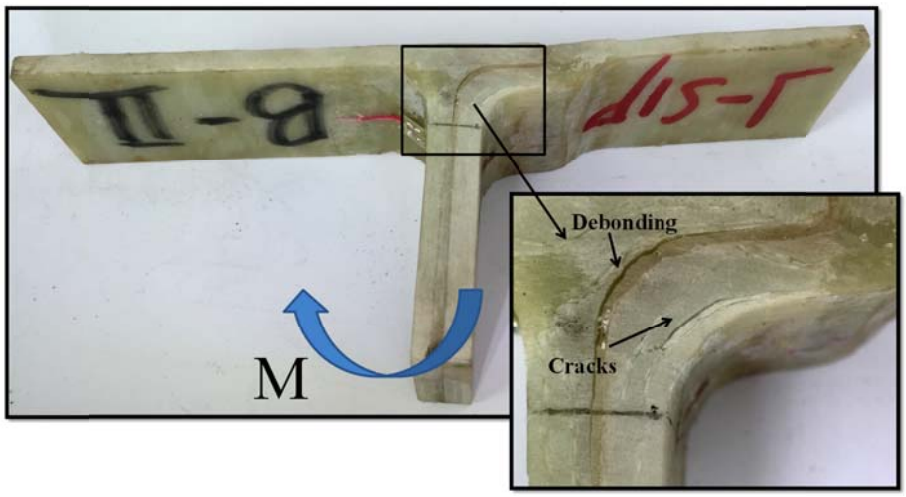

(b) Specimen *AJ1-M2*

Figure (13): Failure modes of adhesively-bonded junction specimen *AJ1*

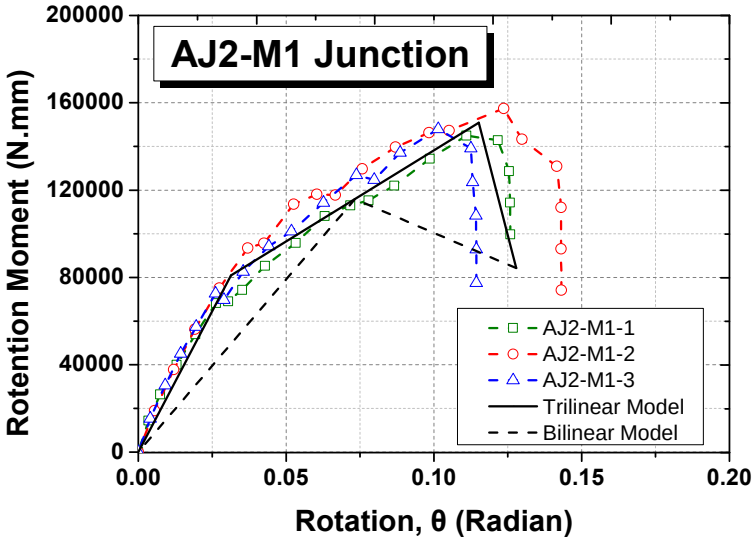

(a) Specimen AJ2-M1

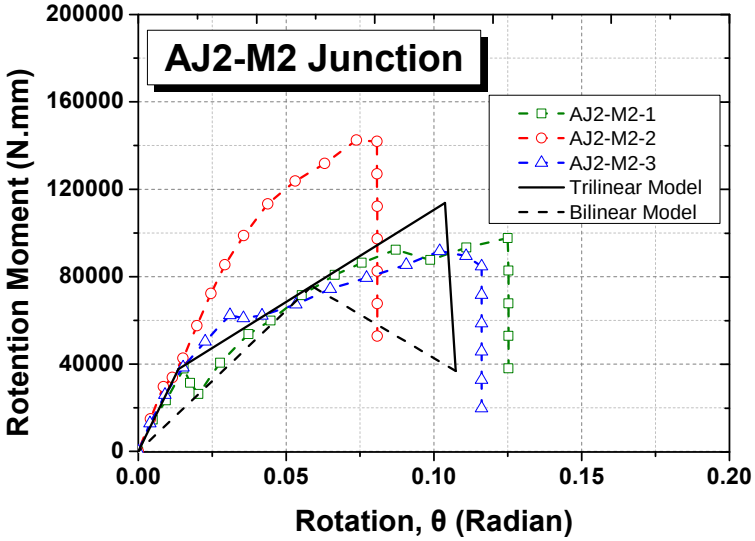

(b) Specimen AJ2-M2

Figure (14): Applied moment versus rotational angle of adhesively-bonded junction specimen *AJ2*

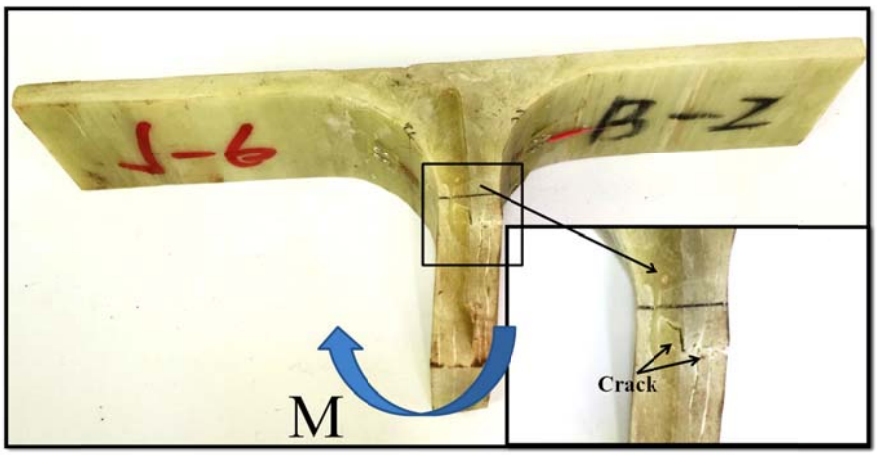

(a) Specimen AJ2-M1

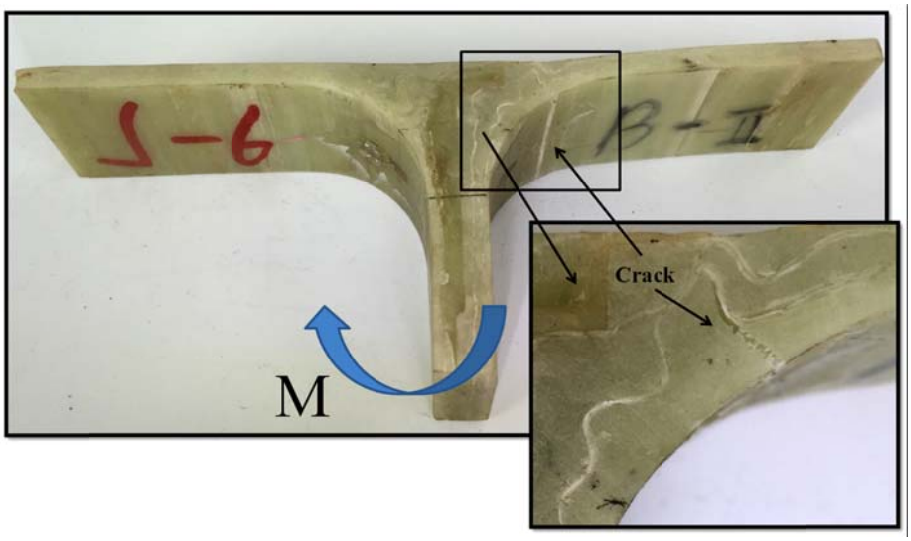

(b) Specimen AJ2-M2

Figure (15): Failure modes of adhesively-bonded junction specimen *AJ2*

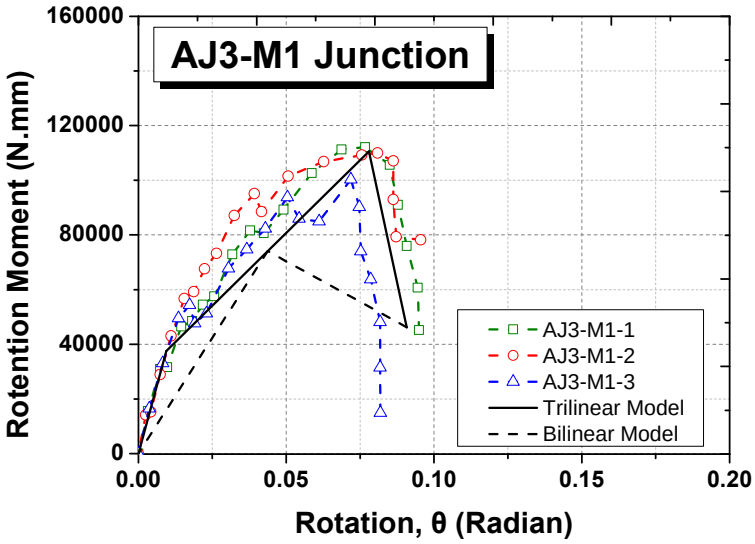

(a) Specimen AJ3-M1

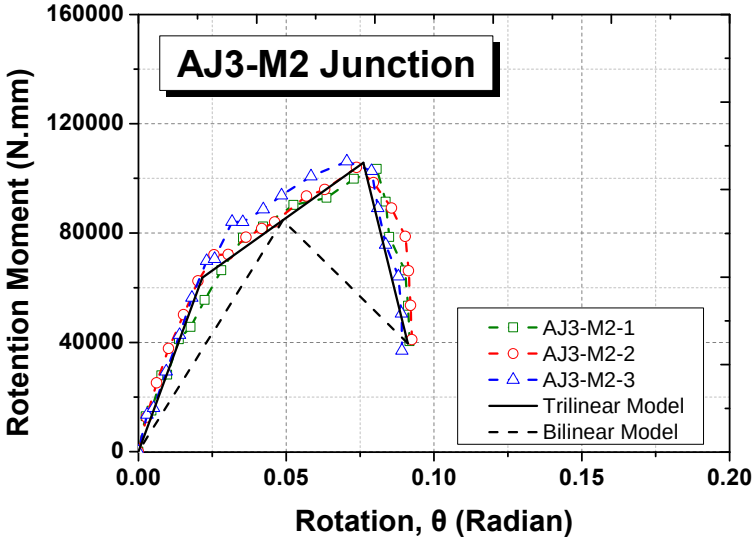

(b) Specimen AJ3-M2

Figure (16): Applied moment versus rotational angle of adhesively-bonded junction specimen *AJ3*

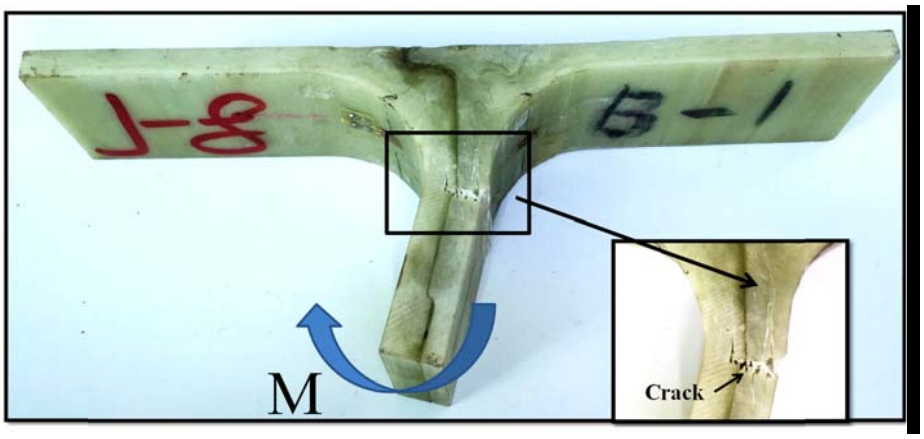

(a) Specimen AJ3-M1

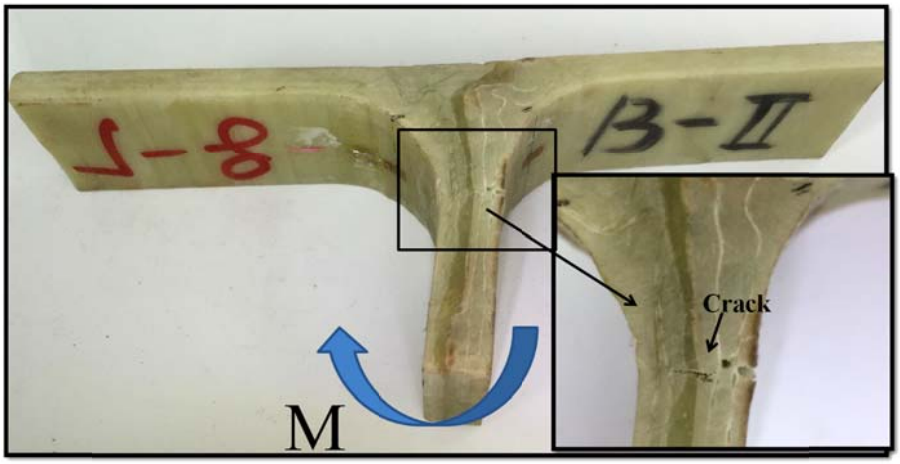

(b) Specimen AJ3-M2

Figure (17): Failure modes of adhesively-bonded junction specimen *AJ3*

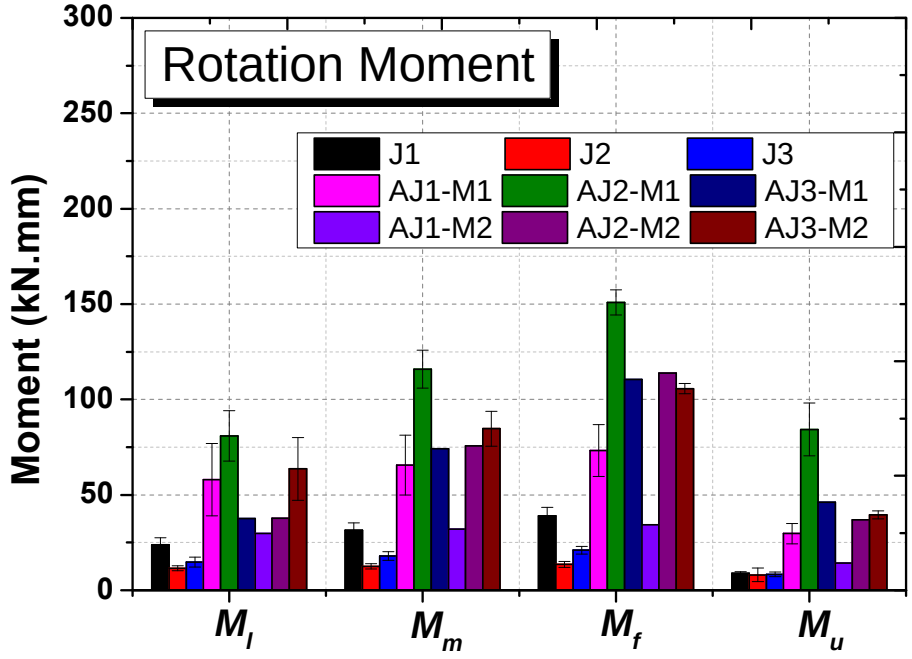

(a) Applied moment

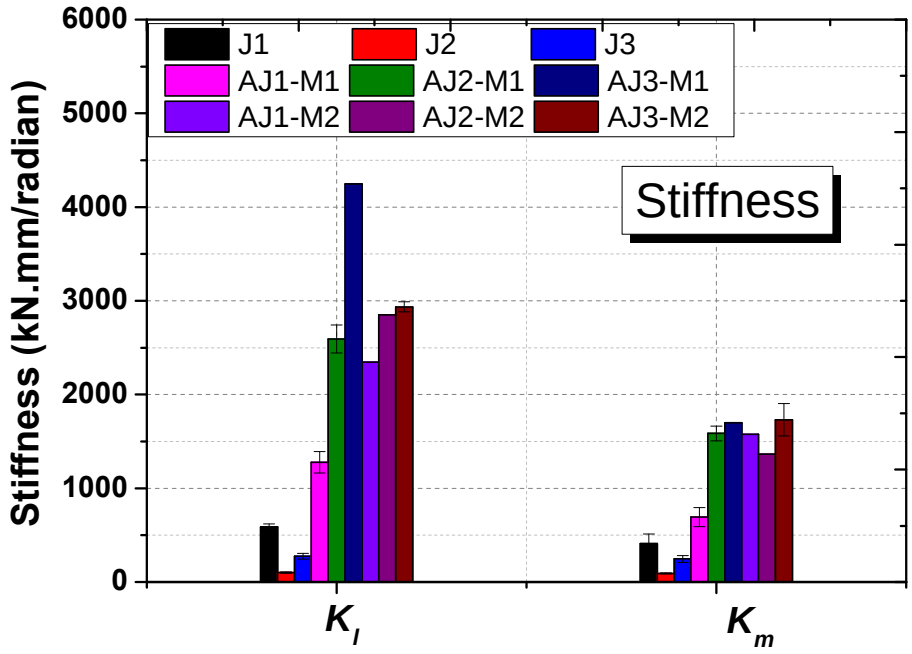

(b) Rotational stiffness

Figure (18): Applied moment and rotational stiffness of different web-flange junctions

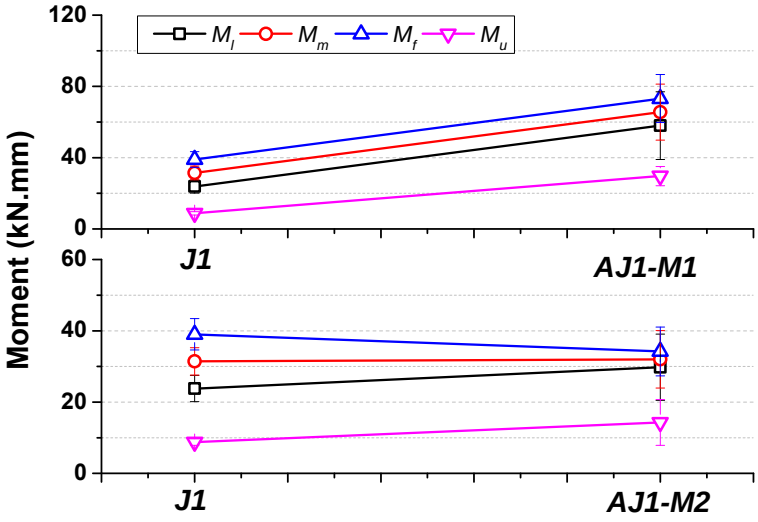

(a) Specimen *J1-AJ1*

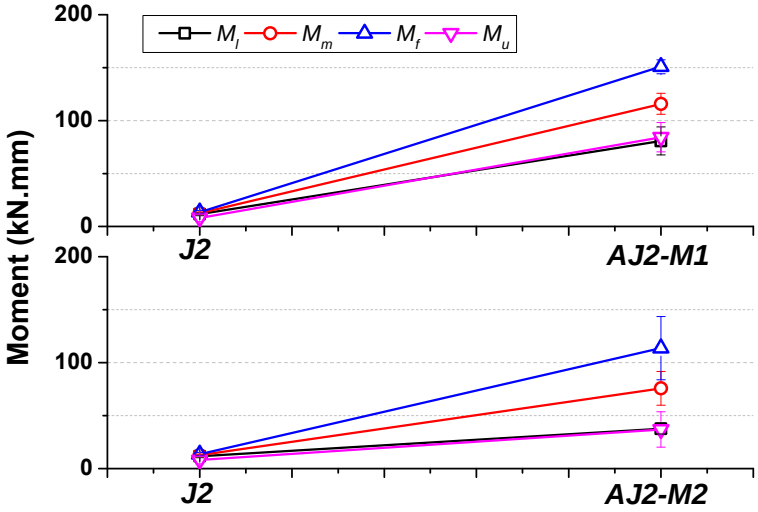

(b) Specimen *J2-AJ2*

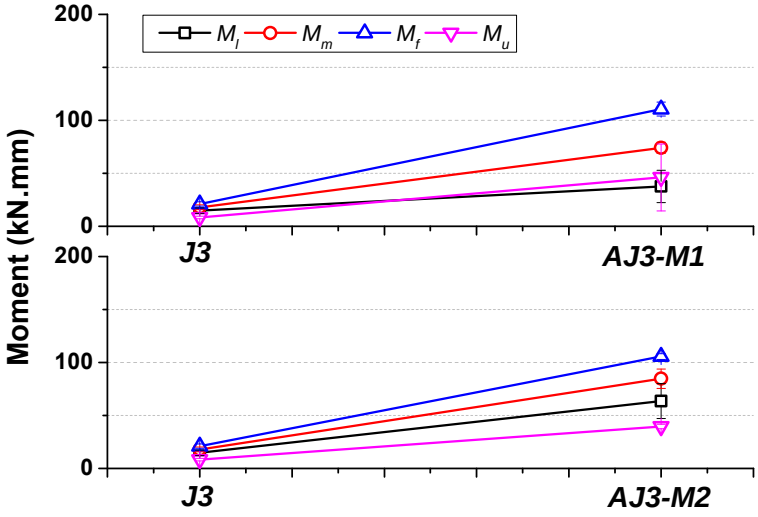

(c) Specimen *J3-AJ3*

Figure (19): Web thickness effects on junctions' moment capacity

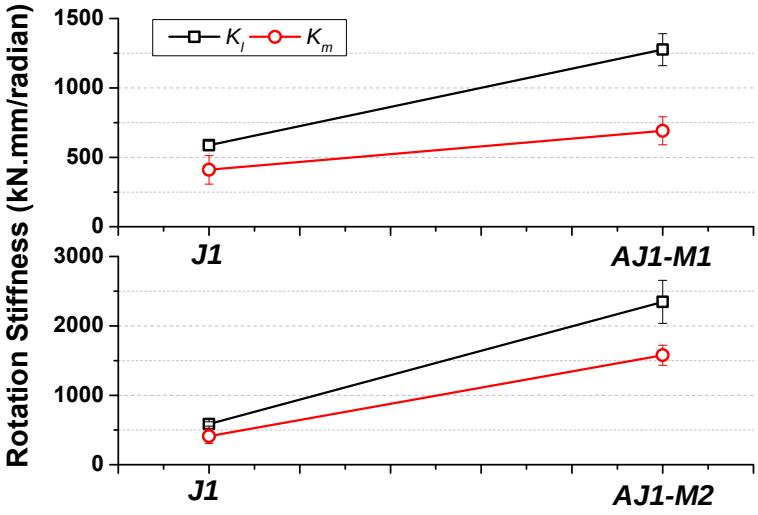

(a) Junction Specimen J1-AJ1

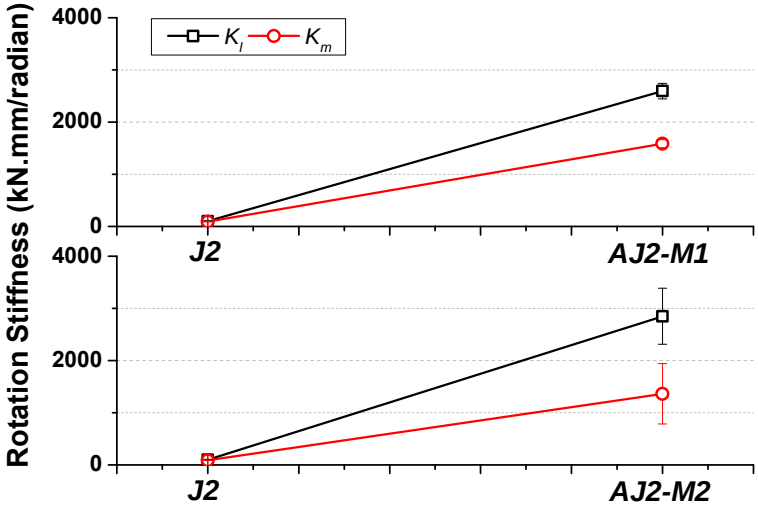

(b) Junction Specimen J2-AJ2

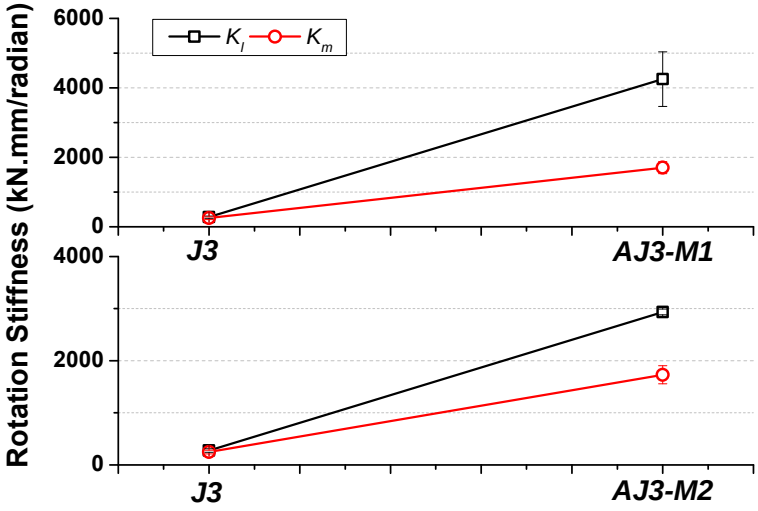

(c) Junction Specimen J3-AJ3

Figure (20): Web thickness effects on rotational stiffness

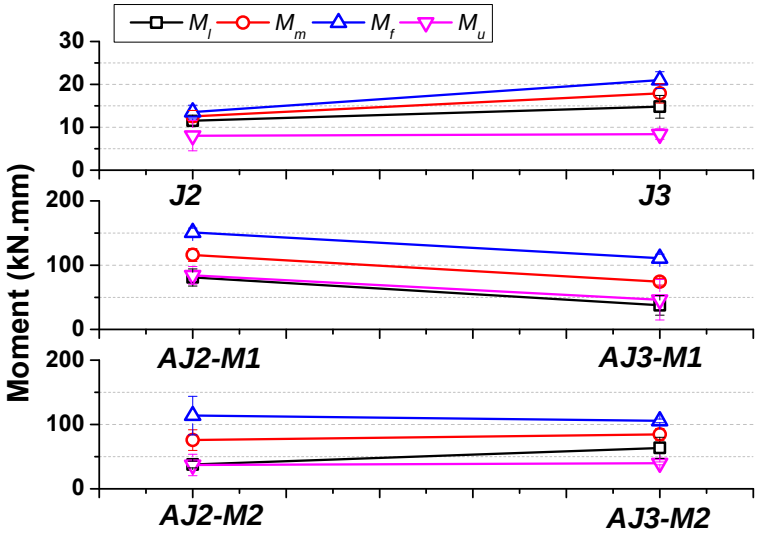

(a) Moment capacity

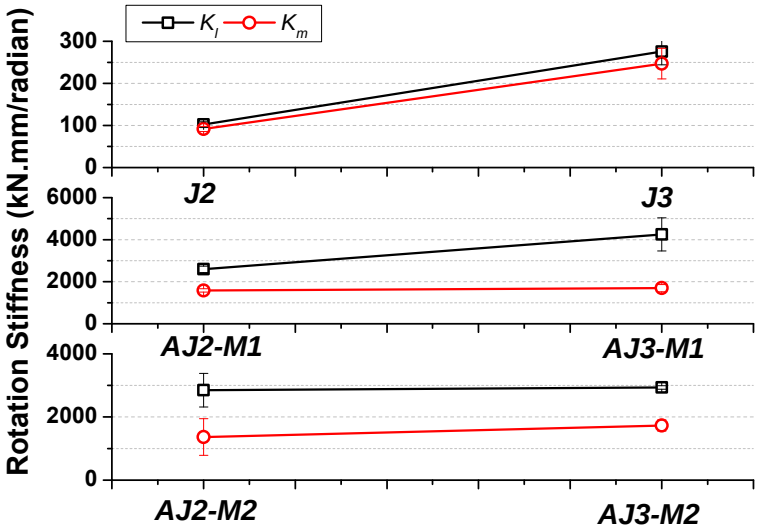

b) Rotational stiffness

Figure (21): Flange thickness effects on rotational moment capacity and rotational stiffness of different pultruded WFJs

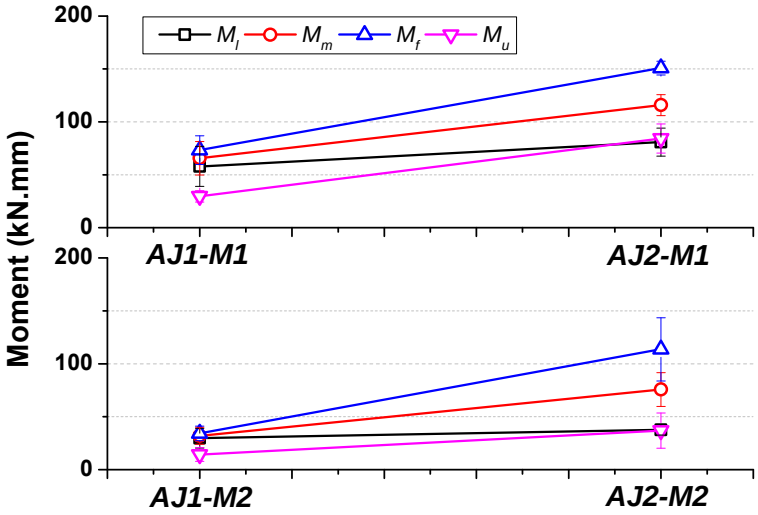

(a) Moment capacity

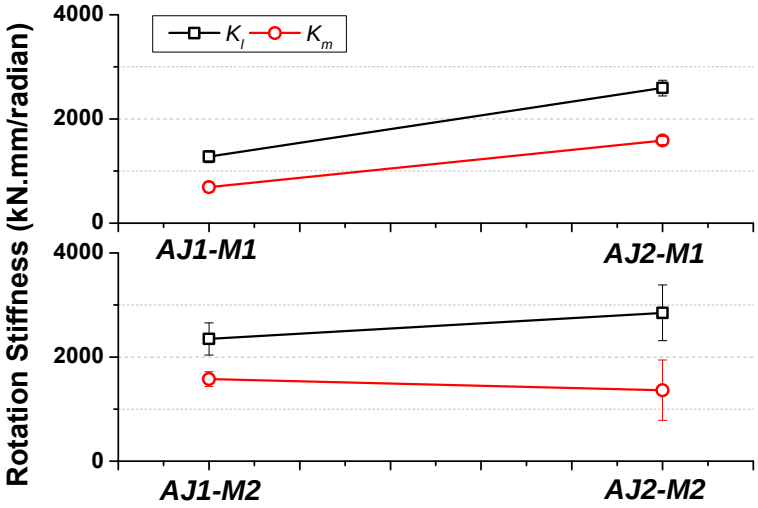

(b) Rotational stiffness

Figure (22): Fillet Radius effects on moment capacity and rotational stiffness of different pultruded WFJs

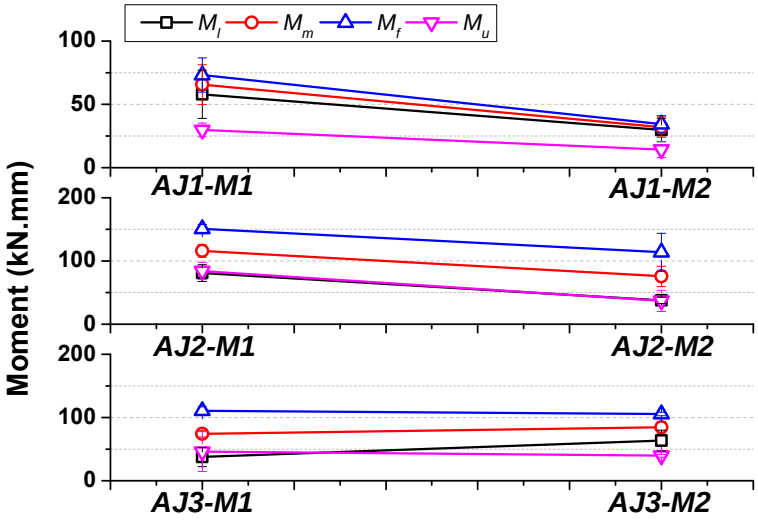

(a) Moment capacity

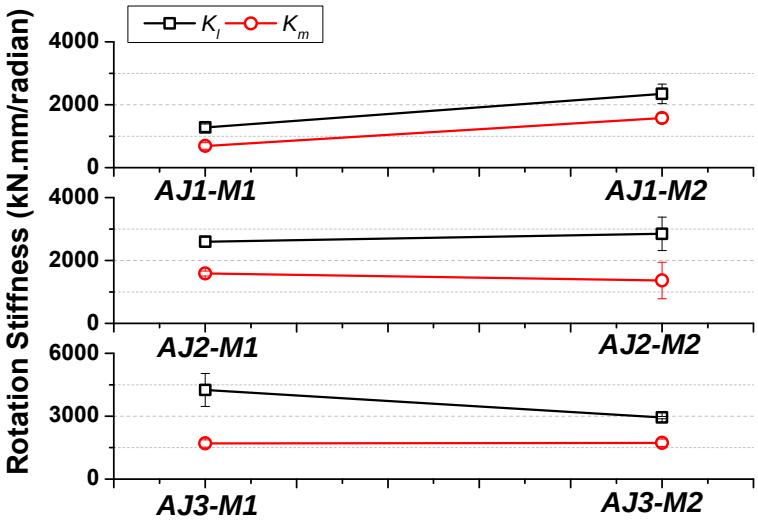

(b) Rotational stiffness

Figure (23): Load direction effects on moment capacity and rotational stiffness of different pultruded WFJs

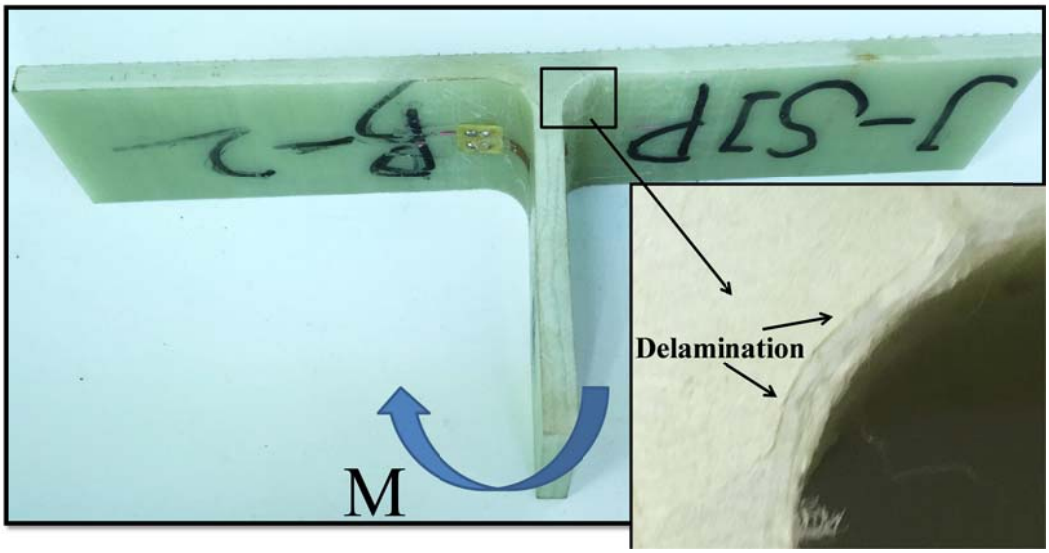

(a) Before hygrothermal aging

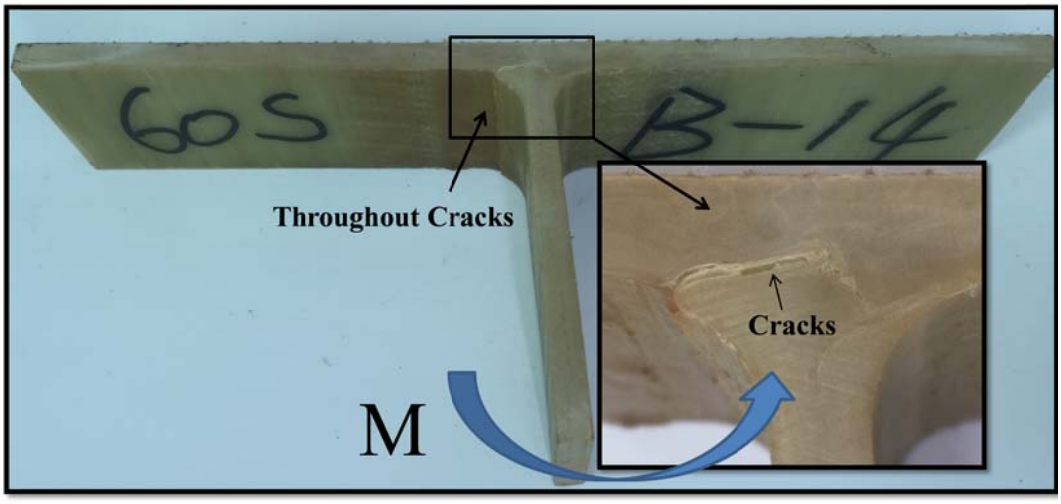

(b) After hygrothermal aging

Figure (24): Typical failure modes comparisons before and after hygrothermal aging

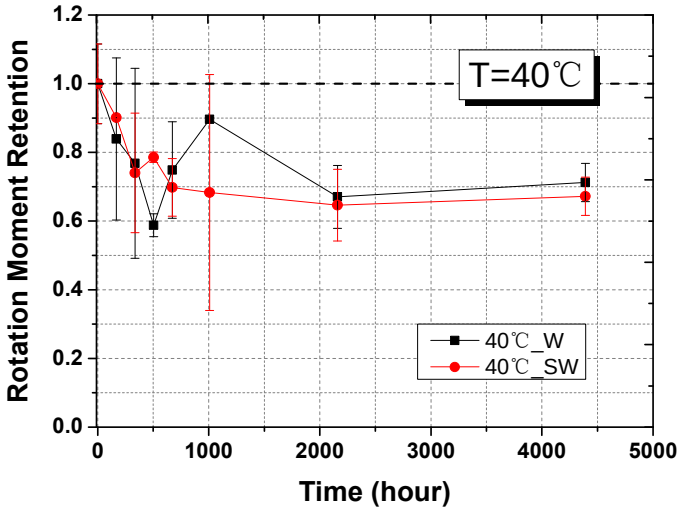

(a) at 40 ℃

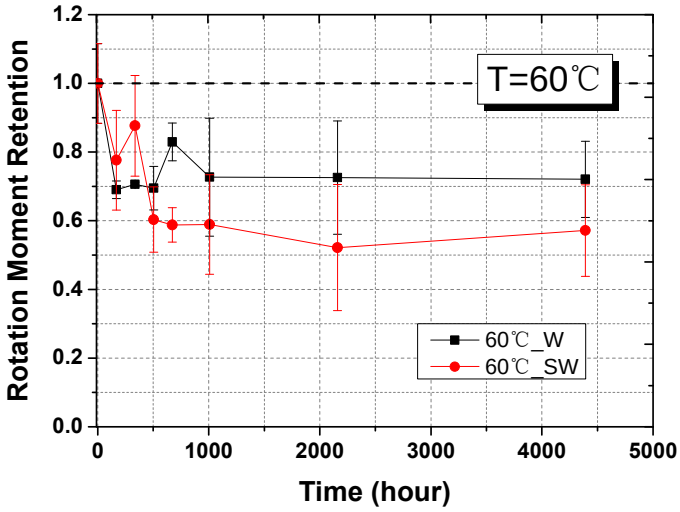

(b) at 60 ℃

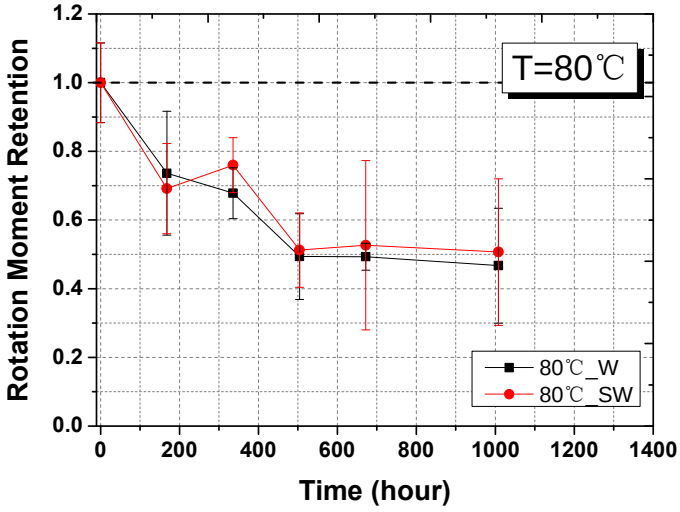

(c) at 80 ℃

Figure (25): Hygrothermal environment (fresh & sea water/temperature) effects on junctions' ultimate moment capacity

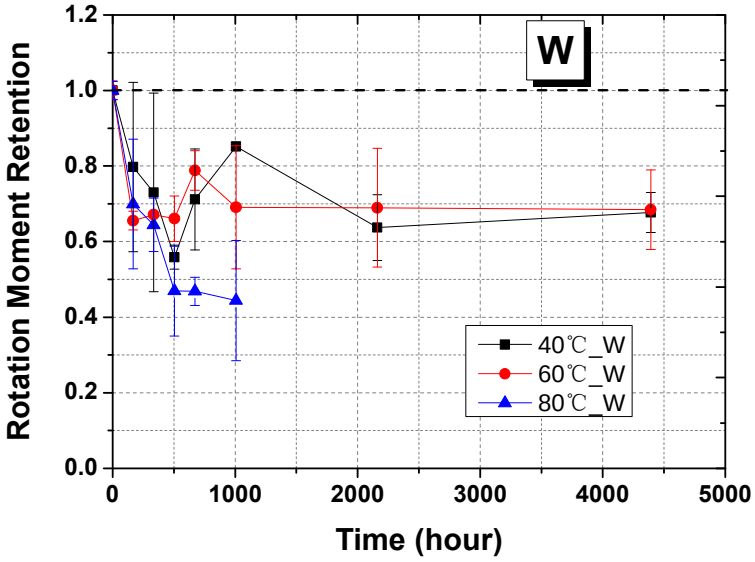

(a) Freshwater environment

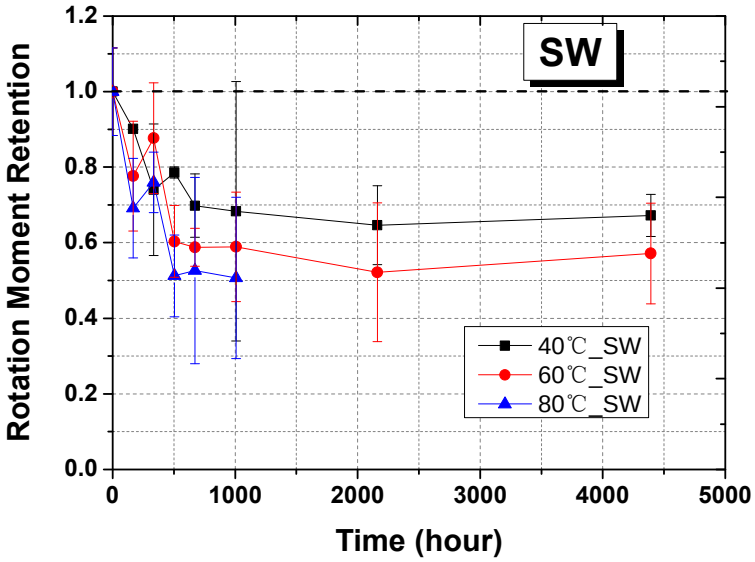

(b) Artificial seawater environment

Figure (26): Hygrothermal temperatures effects on junctions' ultimate moment capacity

LIST OF TABLES

Table 1: Web-flange junction specimens (*Units: mm*)

Specimen ID	*a*	*h*	b_1	b_2	t_f	t_w	*R*
J1	200	86	40	40	6	6	10
J2	200	86	40	40	6	4.5	20
J3	200	88	40	40	8	4.5	20
AJ1	200	86	40	40	6	12.5	10
AJ2	200	86	40	40	6	12.5	30
AJ3	200	88	40	40	8	12.5	30

Table 2: Rotation experimental results of Specimen *J1*

Specimen ID	Moment (kN·mm)				Rotational angle (radian)				Rotational Stiffness (kN·mm/radian)	
	M_l	M_m	M_f	M_u	θ_l	θ_m	θ_f	θ_u	K_l	K_m
J1-1	23.75	32.78	41.81	9.47	0.0394	0.0962	0.1529	0.1537	602.64	340.86
J1-2	27.52	34.42	41.33	8.11	0.0499	0.0952	0.1405	0.1441	551.40	361.49
J1-3	20.15	27.04	33.94	--	0.0332	0.0513	0.0694	--	606.87	527.19
Average	23.81	31.42	39.03	8.79	0.041	0.081	0.121	0.149	586.97	409.85
SD	3.68	3.87	4.41	0.96	0.008	0.026	0.045	0.007	30.87	102.15

Table 3: Rotation experimental results of specimen *J2*

Specimen ID	Moment (kN·mm)				Rotational angle (radian)				Rotational Stiffness (kN·mm/radian)	
	M_l	M_m	M_f	M_u	θ_l	θ_m	θ_f	θ_u	K_l	K_m
J2-1	12.97	14.10	15.23	5.78	0.1179	0.1449	0.1720	0.1707	109.99	97.29
J2-2	11.18	11.58	11.97	6.24	0.1141	0.1351	0.1560	0.2198	98.00	85.71
J2-3	10.55	12.03	13.51	12.15	0.1073	0.1309	0.1545	0.1563	98.31	91.90
Average	11.57	12.57	13.57	8.06	0.1131	0.1370	0.1608	0.1823	102.10	91.63
SD	1.26	1.35	1.63	3.55	0.0054	0.0072	0.0097	0.0333	6.84	5.79

Table 4: Rotational experimental results of specimen *J3*

Specimen ID	Moment (kN·mm)				Rotational angle (radian)				Rotational Stiffness (kN·mm/radian)	
	M_l	M_m	M_f	M_u	θ_l	θ_m	θ_f	θ_u	K_l	K_m
J3-1	12.08	15.81	19.54	7.57	0.0502	0.0765	0.1028	0.1212	240.54	206.67
J3-2	17.37	20.32	23.26	9.27	0.0608	0.0793	0.0978	0.1192	285.79	256.24
J3-3	15.00	17.61	20.22	--	0.0498	0.0635	0.0771	--	300.98	277.37
Average	14.82	17.91	21.01	8.42	0.0536	0.0731	0.0926	0.1202	275.77	246.76
SD	2.65	2.27	1.98	1.20	0.0062	0.0084	0.0136	0.0014	31.44	36.29

Table 5: Rotation experimental results of specimen *AJ1-M1*

Specimen ID	Moment (kN·mm)				Rotational angle (radian)				Rotational Stiffness (kN·mm/radian)	
	M_l	M_m	M_f	M_u	θ_l	θ_m	θ_f	θ_u	K_l	K_m
AJ1-M1 -1	77.58	79.74	81.90	32.90	0.0676	0.1013	0.1351	0.2088	1147.57	786.91
AJ1-M1 -2	56.68	68.45	80.22	32.67	0.0432	0.0976	0.1521	0.2279	1313.19	700.97
AJ1-M1 -3	39.64	48.64	57.63	23.53	0.0290	0.0830	0.1370	0.2167	1367.74	586.00
Average	57.96	65.61	73.25	29.70	0.047	0.094	0.141	0.218	1276.17	691.30
SD	19.00	15.74	13.55	5.35	0.020	0.010	0.009	0.010	114.66	100.80

Table 6: Rotation experimental results for specimen *AJ1-M2*

Specimen ID	Moment (kN·mm)				Rotational angle (radian)				Rotational Stiffness (kN·mm/radian)	
	M_l	M_m	M_f	M_u	θ_l	θ_m	θ_f	θ_u	K_l	K_m
AJ1-M2-1	25.64	28.48	31.32	12.10	0.0104	0.0202	0.0300	0.0333	2,463.62	1,410.38
AJ1-M2-2	23.24	26.29	29.34	9.21	0.0116	0.0158	0.0199	0.0373	1,995.19	1,666.88
AJ1-M2-3	40.42	41.24	42.07	21.49	0.0157	0.0249	0.0342	0.0346	2,579.45	1,653.11
Average	29.77	32.00	34.24	14.27	0.013	0.020	0.028	0.035	2,346.09	1,576.79
SD	9.30	8.07	6.85	6.42	0.003	0.005	0.007	0.002	309.35	144.28

Table 7: Rotation experimental results for specimen *AJ2-M1*

Specimen ID	Moment (kN·mm)				Rotational angle (radian)				Rotational Stiffness (kN·mm/radian)	
	M_l	M_m	M_f	M_u	θ_l	θ_m	θ_f	θ_u	K_l	K_m
AJ2-M1-1	71.67	108.82	145.98	100.12	0.0282	0.0704	0.1127	0.1261	2,540.73	1544.83
AJ2-M1-2	95.99	127.17	158.35	74.92	0.0388	0.0828	0.1268	0.1430	2,476.44	1536.67
AJ2-M1-3	74.92	111.58	148.24	77.76	0.0271	0.0666	0.1061	0.1144	2,761.90	1675.58
Average	80.86	115.86	150.86	84.27	0.031	0.073	0.115	0.128	2,593.03	1585.69
SD	13.21	9.89	6.58	13.80	0.006	0.008	0.011	0.014	149.74	77.95

Table 8: Rotation experimental results for specimen *AJ2-M2*

Specimen ID	Moment (kN·mm)				Rotational angle (radian)				Rotational Stiffness (kN·mm/radian)	
	M_l	M_m	M_f	M_u	θ_l	θ_m	θ_f	θ_u	K_l	K_m
AJ2-M2-1	41.86	70.44	99.02	38.05	0.0176	0.0704	0.1232	0.1252	2,384.01	1000.94
AJ2-M2-2	39.30	93.72	148.14	52.94	0.0114	0.0462	0.0809	0.0809	3,434.59	2030.74
AJ2-M2-3	31.99	63.02	94.06	19.61	0.0117	0.0595	0.1072	0.1160	2,729.80	1059.82
Average	37.72	75.73	113.74	36.87	0.014	0.059	0.104	0.107	2,849.47	1363.83
SD	5.12	16.02	29.89	16.70	0.003	0.012	0.021	0.023	535.41	578.31

Table 9: Rotation experimental results for specimen *AJ3-M1*

Specimen ID	Moment (kN·mm)				Rotational angle (radian)				Rotational Stiffness (kN·mm/radian)	
	M_l	M_m	M_f	M_u	θ_l	θ_m	θ_f	θ_u	K_l	K_m
AJ3-M1-1	38.96	76.51	114.06	45.18	0.0096	0.0415	0.0734	0.0950	4,041.39	1,843.83
AJ3-M1-2	21.63	68.15	114.67	78.14	0.0042	0.0452	0.0861	0.0956	5,116.16	1,508.37
AJ3-M1-3	52.02	77.51	103.00	15.14	0.0145	0.0446	0.0747	0.0819	3,584.86	1,738.40
Average	37.53	74.06	110.58	46.15	0.009	0.044	0.078	0.091	4,247.47	1,696.87
SD	15.25	5.14	6.57	31.51	0.005	0.002	0.007	0.008	786.18	171.54

Table 10: Rotation experimental results for specimen *AJ3-M2*

Specimen ID	Moment (kN·mm)				Rotational angle (radian)				Rotational Stiffness (kN·mm/radian)	
	M_l	M_m	M_f	M_u	θ_l	θ_m	θ_f	θ_u	K_l	K_m
AJ1-M2-1	44.64	74.15	103.66	40.34	0.0153	0.0482	0.0810	0.0917	2,917.17	1539.49
AJ1-M2-2	73.02	88.79	104.57	41.13	0.0252	0.0499	0.0745	0.0926	2,891.93	1779.75
AJ1-M2-3	73.25	91.03	108.81	37.21	0.0244	0.0486	0.0727	0.0892	2,996.22	1873.32
Average	63.64	84.66	105.68	39.56	0.022	0.049	0.076	0.091	2,935.11	1730.85
SD	16.45	9.17	2.75	2.08	0.006	0.001	0.004	0.002	54.41	172.20

Table 11: Ultimate moment variation of specimen *J1* exposed to freshwater environment

Time (hours)	40℃_W (kN·mm)		60℃_W (kN·mm)		80℃_W (kN·mm)	
	Mea	SD	Average Value	SD	Average Value	SD
0	39.04	4.41	39.04	4.41	39.04	4.41
168	35.19	0.13	26.93	1.01	28.73	7.04
336	28.91	6.80	27.58	0.23	26.47	2.89
504	30.68	0.59	27.14	2.47	19.27	4.88
672	27.26	3.29	32.38	2.15	19.25	1.53
1,008	26.68	13.40	28.38	6.70	18.24	6.54
2,160	25.23	4.07	28.34	6.44	--	--
4,392	26.24	2.18	28.13	4.33	--	--

Table 12: Ultimate moment variation of specimen *J1* exposed to artificial seawater environment

Time (hours)	40℃_SW (kN·mm)		60℃_SW (kN·mm)		80℃_SW (kN·mm)	
	Average Value	SD	Average Value	SD	Average Value	SD
0.0	39.04	4.41	39.04	4.41	39.04	4.41
168.0	32.77	9.22	30.31	5.67	27.00	5.13
336.0	29.99	10.80	34.22	5.72	29.67	3.12
504.0	22.95	1.30	23.55	3.71	20.01	4.23
672.0	29.23	5.50	22.95	1.95	20.56	9.63
1,008.0	34.98	0.23	23.00	5.66	19.78	8.33
2,160.0	26.17	3.58	20.38	7.16	--	--
4,392.0	27.81	2.18	22.31	5.20	--	--